Review

Israel Journal of Chemistry

DOI: 10.1002/ijch.201400079

Fundamentals and Modeling of Electrokinetic Transport in Nanochannels

Hung-Chun Yeh,[a] Moran Wang,[b] Chih-Chang Chang,[c] and Ruey-Jen Yang*[a]

Abstract: When the channel size approaches the thickness of the charged layer (typically, ~10–100 nm), the resulting molecular and non-equilibrium effects are markedly different from those observed in larger channels and have a significant effect on the transport behavior of solutes and solvents. As a result, the problem of modeling fluidic behavior at the nanoscale has attracted increasing interest in recent years. This review introduces the fundamental theories and principles associated with electrokinetic transport and molecular dynamics modeling, and discusses various applications of nanofluidic devices in the physics, mechanics, and chemistry fields.

Keywords: electrokinetic transport · electroosmotic flow · nanochannels · nanotechnology · nanotubes

1 Introduction

Fluid flow through internal channel passages occur in many common applications, ranging from large-scale engineering piping systems to biological nanoscale ion channels. Nanofluidics is defined as the study and application of fluid flow in and around nano-sized objects, with at least one characteristic dimension of less than 100 nm. At such small characteristic scales, the nanostructures have a high surface-to-volume ratio, resulting in many new and interesting physical phenomena and applications. Consequently, the nanofluidics field has attracted great interest in the academic and research communities in recent decades. Of the various phenomena observed at the nanoscale, the transport of a fluid within a nanochannel, via the application of an external electrical gradient, has many potential applications in the biomedical, energy, and environmental fields. Consequently, the problem of electrokinetic transport in nanochannels has attracted particular attention in the recent literature.

The transport of a fluid confined in a nanochannel must consider its associated geometric length scales. It was shown in Refs. [1–4] that for nanoscale lengths greater than 1 nm (equivalent to the thickness of approximately three water molecule layers), fluid flow obeys the continuum assumption and can therefore be described using the conventional Navier-Stokes equation. Furthermore, it was reported in Refs. [5–7] that the characteristic length scale of nanoscale applications depends on the variation of intermolecular forces near the nanochannel surface, which is governed, in turn, by the steric interaction/hydration, van der Waals, and electrostatic phenomena, with characteristic scales of 1–2 nm,1–10 nm, and 10–100 nm, respectively. Micro/nanofluidic devices are generally fabricated on dielectric substrates such as silicon, glass, polydimethylsiloxane (PDMS), or some other form of polymer. When an electrolyte solution passes through a nanochannel, the material surface has charges distributed on it by the dissociation of surface groups and by the specific (nonelectric) adsorption of ions from the solution to the surface to form the so-called surface charge density, and an electrical double layer (EDL) is formed. At the small characteristic scale associated with nanofluidic devices, the EDL results in many new physical phenomena, including the EDL overlap condition,[8] the ion exclusion-enrichment (EEE) effect,[9] and ion concentration polarization (ICP).[10,11] These phenomena have made possible the development of many new and exciting applications in recent decades, including selective macromolecular sieves,[12] pre-concentration devices,[13,14] ion-selective transport systems,[15] nanofluidic transistors,[6,16] nanofluidic diodes,[17] electrokinetic batteries,[18,19] and desalination systems.[20,21] However, in optimizing the performance of

[a] H.-C. Yeh, R.-J. Yang
Department of Engineering Science
National Cheng Kung University
Tainan, 701 (Taiwan)
e-mail: rjyang@mail.ncku.edu.tw

[b] M. Wang
Department of Engineering Mechanics and CNMM
School of Aerospace
Tsinghua University
Beijing, 100084 (P. R. China)

[c] C.-C. Chang
Green Energy and Environment Research Laboratories
Industrial Technology Research Institute
Hsinchu, 310 (Taiwan)

© 2014 Wiley-VCH Verlag GmbH & Co. KGaA, Weinheim

such applications, a detailed understanding of the electrokinetic transport phenomenon is required.

Accordingly, this study presents a systematic review of the electrokinetic transport phenomenon and its modeling by means of numerical simulations. The paper is organized as follows. Section 2 introduces the fundamental theories and principles associated with the electrokinetic transport effect. Section 3 describes the theories and assumptions involved in modeling the electrokinetic transport phenomenon in the continuum and non-continuum domains. Section 4 illustrates some applications of electrokinetic flow over the past decade or so. Finally, Section 5 provides some brief concluding remarks. This review is our subjective view and therefore cannot be exhaustive.

2 Principles of Electrokinetic Fluid Dynamics

The electrokinetic (EK) phenomenon arises from the existence of a non-electroneutral electrical double layer at the liquid-solid interface of a material bearing surface charges, where these charges are generally produced by the chemical adsorption or dissociation of the surface functional groups following contact with an aqueous solution. The EK effect plays a particularly critical role in promoting ion transport in nanochannels due to their extremely high surface-to-volume ratio, and results in many interesting phenomena, including electroosmotic flow (EOF),[22,23] electroviscosity,[24] and electroconvection.[25] In this section, the basic principles and theories of EK flow in nanofluidic channels are briefly reviewed.

2.1 Length Scales

Broadly speaking, the Debye length describes the thickness of the EDL, and is given from Poisson-Boltzmann theory as

Hung-Chun Yeh was born in Hsinchu, Taiwan, in 1985. Currently, he is a Ph.D. student in National Cheng Kung University. His research interest focuses on fuel cell and micro/nanofluidics, especially the electrokinetic energy conversion and its improvement on the conversion efficiency for nanofluidic energy converters.

Moran Wang was born in Jilin, China in 1977. He received his BS degree and Ph.D. degree from the Department of Engineering Mechanics of Tsinghua University in 1999 and 2004, respectively. After graduation, Dr. Wang continued his research on micro- and nano-transport mechanisms at the Johns Hopkins University (2004–2006) and University of California (2006–2008) as a postdoctoral fellow. In 2008, Dr. Wang was awarded the J. Robert Oppenheimer Fellowship by DOE of USA and entered the Los Alamos National Laboratory as an Oppenheimer Fellow. Dr. Wang is now a professor at the School of Aerospace at Tsinghua University. His major research interests are micro/nanoscale transport in energy and environments, multiphysical transport in porous media, and multiscale modeling. Dr. Wang is on editorial boards of several international journals, including *Micro and Nanosystems* and *Journal of Porous Media*.

Chih-Chang Chang was born in Taichung, Taiwan, in 1979. He received his Ph.D. degree from the Department of Engineering Science, National Cheng Kung University (NCKU), in 2007. From 2008–2012, he worked as a postdoctoral fellow at NCKU. In 2012, he was a visiting postdoctoral scholar at the Department of Applied Chemistry, the University of Tokyo. Currently, he is a researcher at the Green Energy and Environment Research Laboratories, Industrial Technology Research Institute (ITRI), Hsinchu, Taiwan. His research focuses on energy-efficient air conditioning systems, air pollution prevention, energy harvesting, microfluidics/nanofluidics, and electrokinetics.

Ruey-Jen Yang is a Chair Professor of Engineering Science at National Cheng Kung University (NCKU) in Taiwan. He received his Ph.D. degree in Mechanical Engineering from the University of California, Berkeley in 1982. He has been with the NCKU since 1993, after 11 years of service in the USA. His research interest includes micro/nanofluidics and fluid/thermal sciences. Dr. Yang is on editorial boards of several international journals, including *Microfluidics and Nanofluidics*.

© 2014 Wiley-VCH Verlag GmbH & Co. KGaA, Weinheim

Israel Journal of Chemistry

$$\lambda_D = \sqrt{\frac{\varepsilon_0 \varepsilon_f RT}{F^2 \sum_i c_i^\infty z_i^2}}, \quad (1)$$

where the z_i is the valence, c_i^∞ is the bulk concentration, F is the Faraday constant, R is the gas constant, T is the absolute temperature, ε_0 is the permittivity of a vacuum, and ε_f is the dielectric constant of the electrolyte solution. As shown in Eq. (1), the Debye length varies inversely with the bulk ion concentration. For example, given a dilute ion concentration, the Debye length is very large and may even approach infinity ($\lambda_D \to \infty$). Thus, in practical applications, the width of the diffuse layer is assumed to be fixed by the so-called Gouy-Chapman length, defined as

$$\lambda_{GC} = \frac{2\varepsilon_0 \varepsilon_f RT}{z_+ F|\sigma_s|}, \quad (2)$$

where σ_s is the surface charge density. Basically, the Gouy-Chapman length defines the region of the channel over which most of the counter-ions in the electrolyte are concentrated, as a result of surface charge effects. Finally, the Dukhin length quantifies the relationship between the bulk electrical conductance and the surface electrical conductance, and is defined as

$$l_D = \frac{|\sigma_s|}{z_+ F c_i^\infty}. \quad (3)$$

The Dukhin length is commonly rewritten in terms of the Debye and Gouy-Chapman lengths as $l_D \approx \lambda_D^2/\lambda_{GC}$, and provides an important indication of the electrical conductance of the nanochannel given a dilute bulk concentration. The Dukhin length is also commonly divided by the height of the nanochannel and expressed in the form of a dimensionless parameter known as the Dukhin number, i.e.,

$$Du = \frac{c_e}{c_i^\infty} = \frac{|\sigma_s|}{h z_+ F c_i^\infty}, \quad (4)$$

where $c_e = |\sigma_s|/h z_+ F$ is the surface charge in the nanochannel. The Dukhin number provides an indication of both the ion-selectivity of the nanochannel and the dominant conductance mechanism. For example, given $Du \gg 1$, the nanochannel is ion-selective and the conductance is dominated by the surface charge density.

Traditionally, fluid flow in a nanochannel is assumed to be bounded by a no-slip condition at the wall. However, recent studies have shown that liquid slip actually occurs on bare (atomically smooth) surfaces at the micro/nanoscale, particularly in the case of superhydrophobic surfaces.[26] It has been reported that this slippage may be due either to molecular (i.e., intrinsic) slip on the bare surface or to apparent slip on the structure surface.[27] Thus, the flow velocity at the channel wall is more properly described using the following Navier slip boundary condition:

$$u_s = b\left(\frac{du}{dy}\right), \quad (5)$$

where $b = \eta/\lambda$ is the slip length, in which η is the fluid viscosity and λ is the friction coefficient. In practice, the slip length and friction coefficient are both strongly dependent on the intensity of the intermolecular interactions between the solid surface and the liquid.

2.2 Electrical Double Layer/Electroosmotic Flow

Many solid substrate materials (e.g., plastic and glass) acquire an electric charge when they come into contact with an aqueous solution. When an aqueous solution is in contact with the substrate material of a solid-state nanochannel, such as silicone dioxide (SiO_2), it reveals a charge-regulated nature due to the protonation/deprotonation surface reaction. This implies that the surface charge property of the nanochannel depends strongly on the local concentration of the hydrogen ions (i.e., a pH value effect) on its surface.[28–30] These surface charges attract the counter-ions within the aqueous solution while simultaneously repulsing the co-ions. The counter-ions are adsorbed on the charged surface via electrostatic effects, resulting in the formation of an electrical double layer comprising a compact layer and a diffuse layer (see Figure 1). In general, the thickness of the EDL is determined by the Debye length, i.e., $\lambda_D \propto 1/\sqrt{c_i^\infty}$, where c_i^∞ is the bulk ion concentration. In other words, for a high ion concentration, the EDL has only a thin thickness; allowing both the co-ions and the counter-ions to pass readily through the channel. Conversely, for a low ionic strength, the EDL thickness increases, with the result that the nanochannel becomes counter-ion selective. Notably, when the Debye length approaches the width of the nanochannel, an overlap of the EDLs on the opposite walls occurs. In such cases, the counter-ion concentration in the double layer region is greater than that of the co-ion concentration. In other words, the ion concentration in the middle of the channel is given by $c_+ \neq c_- \neq c_i^\infty$ and the EDL potential is given as $\psi_0 \neq 0$, as shown in Figure 2.

The presence of the EDL screens (i.e., shields) the ions in the bulk fluid from the effects of the surface charges. In other words, the net charge within the EDL neutralizes the charged surface, and is therefore given by

$$\sigma_s = -\int_0^\infty \rho_e d\mathbf{n}, \quad (6)$$

where σ_s is the surface charge density, $\rho_e = F\sum_i z_i c_i$ is the

© 2014 Wiley-VCH Verlag GmbH & Co. KGaA, Weinheim

Israel Journal of Chemistry

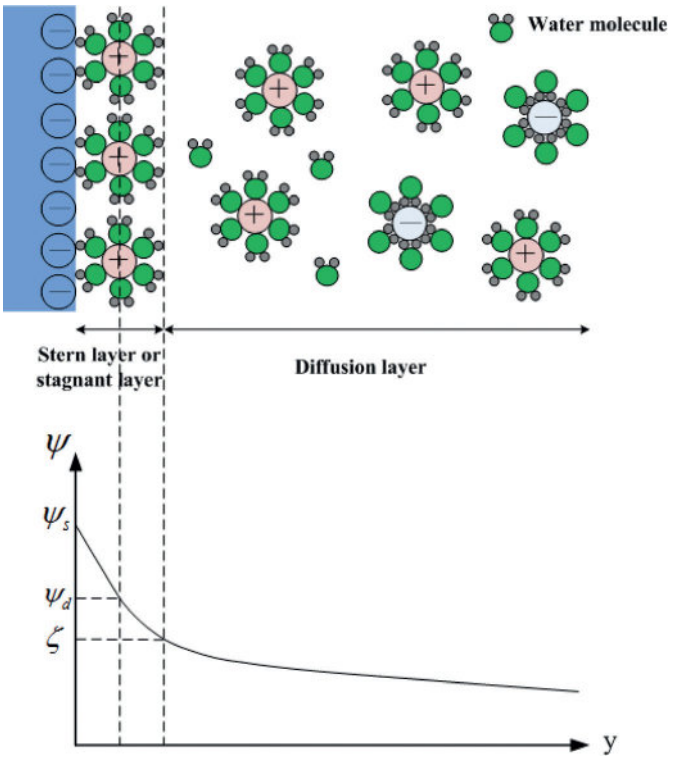

Figure 1. Gouy-Chapman-Stern model of EDL structure.

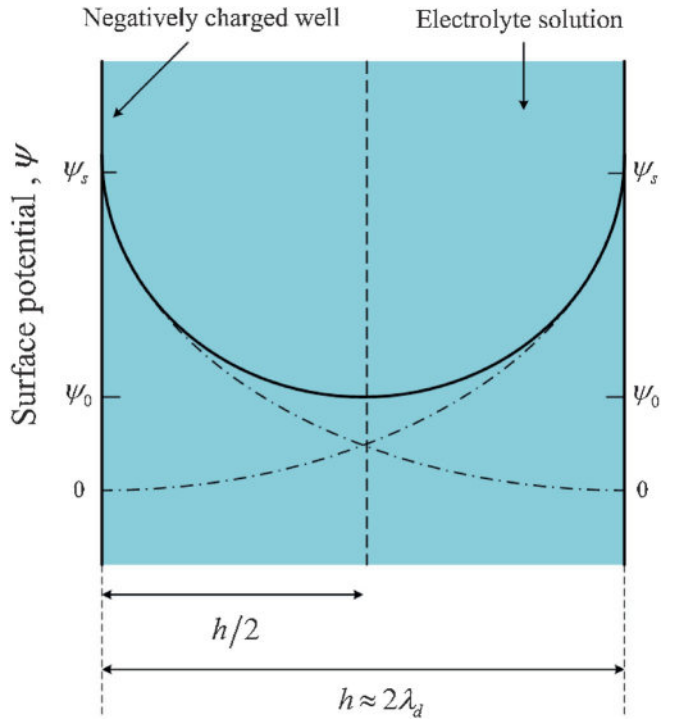

Figure 2. Overlapped EDL condition between pair of charged surfaces separated by distance *h*.

net charge density, and **n** is the direction normal to the surface.

According to electrostatic theory, the electric potential distribution in the channel can be described by the following Poisson equation:

$$\nabla^2\psi = -\frac{\rho_e}{\varepsilon_0\varepsilon_f}, \tag{7}$$

where ρ_e is the net charge density and is given as $\rho_e = F\sum_i z_i c_i$, in which F is the Faraday constant and z_i and c_i are the valence and local molar concentration of the type-i ions, respectively. The concentration of the type-i ions depends on the electrochemical potential (i.e., $\mu_i = \mu_i^0 + RT\ln c_i + z_i F\psi$, where m_i^0 is the standard state chemical potential of the type-i ions, R is the gas constant and T is the absolute temperature) and conforms to the following Boltzmann distribution:

$$c_i = c_i^\infty \exp\left(-\frac{z_i F\psi}{RT}\right). \tag{8}$$

At thermodynamic equilibrium state, employing the Boltzmann distribution to describe ion distribution inside the channel is valid. Substituting Eq. (8) into the Poisson equation (Eq. (7)) yields the following well-known Poisson-Boltzmann (PB) formulation:

$$\nabla^2\psi = -\frac{F}{\varepsilon_0\varepsilon_f}\sum_i c_i^\infty z_i \exp\left(-\frac{z_i F\psi}{RT}\right). \tag{9}$$

The PB equation describes the EDL potential distribution within the nanochannel under equilibrium conditions. Given a symmetrical electrolyte (i.e., $z_i : z_i = 1:1$), and considering only one dimension (i.e., normal to the wall surface), the PB equation can be expressed in the following simplified form:

$$\frac{d\psi}{dy} = \frac{RT}{zF}\kappa^2 \sinh\left(\frac{z_i F\psi}{RT}\right), \tag{10}$$

where $\kappa = \lambda_D^{-1} = \sqrt{2z^2F^2c_i^\infty/(\varepsilon_0\varepsilon_f RT)}$ is the so-called Debye-Hückel parameter. Substituting Eqs. (7) and (10) into Eq. (6), the surface charge density is obtained as

$$\sigma_s = \frac{2z_i F\kappa c_i^\infty}{\varepsilon_0\varepsilon_f}\sinh\left(\frac{z_i F\psi_s}{RT}\right), \tag{11}$$

where the ψ_s is the so-called surface potential. In nanofluidic applications, the surface potential is assumed to be less than the thermal voltage, i.e., $z_i\psi < RT/F$, where $RT/F = 25.7$ mV at 25°. Thus, the following so-called Debye-Hückel approximation is obtained:

$$\nabla^2\psi = \kappa^2\psi. \tag{12}$$

© 2014 Wiley-VCH Verlag GmbH & Co. KGaA, Weinheim

For a symmetrical electrolyte, the potential distribution along the y-axis of the channel is given by

$$\psi(y) = \psi_s \exp(-\kappa y). \tag{13}$$

However, for high surface potentials, the analytical Debye-Hückel approximation cannot be used due to the non-linearity of the PB equation. Accordingly, an exact solution is obtained under the assumption of $d\psi/dy = 0$ at the centerline of the nanochannel, using the following Gouy-Chapman equation:

$$\psi(y) = \frac{2RT}{zF} \ln\left[\frac{1 + \tanh(zF\psi_s/4RT)\exp(-\kappa y)}{1 - \tanh(zF\psi_s/4RT)\exp(-\kappa y)}\right]. \tag{14}$$

In recent years, many researchers have argued that the traditional PB equation cannot be used to describe the overlapped EDL phenomenon in very narrow nanochannels since the electroneutrality assumption of the PB model (i.e., $c_+ = c_- = c_i^\infty$) at the middle plane is invalid. As shown in Figure 2, the overlapped EDL phenomenon is usually modeled as either a closed system or an open system. Qu and Li[31] considered the conservation of the ion number (i.e., salt ions, hydronium ions, and hydroxide ions), the dissociation of water, and surface charge regulation effects (i.e., site dissociation) in an infinitely long channel (i.e., a closed system). However, the surface charge regulation model which they adopted (proposed by Healy and White[32]) was originally derived for an open system. Accordingly, in a more recent study, Baldessari and Santiago[33] developed a new EDL model based on a channel-to-well equilibrium assumption and used this model to derive a semi-analytical solution for the overlapped EDL field. It was shown that the proposed model provided a more accurate description of the overlapped EDL field than the so-called "thick EDL model"[34,35] since the condition of $\psi_0 \neq 0$ was taken into account.

Electroosmotic flow is a micro/nanofluidic phenomenon in which a movement of the bulk liquid, relative to the stationary, charged surface, occurs under the effects of an externally applied electric field. The EOF velocity can be derived in accordance with $\mu d^2u/dy^2 + \rho_x E_x = 0$, where $\mathbf{E}_x = -\nabla\psi$ is the intensity of the electric field and $\rho_x = -\varepsilon_0\varepsilon_f d^2\psi/dy^2$ is the net charge density. Moreover, the boundary conditions are $du/dy = d\psi/dy = 0$ at the middle plane, and $u = 0$ and $\psi = \zeta$ at the channel surface. ζ is the so-called zeta potential. The velocity profile over the height of the nanochannel is given by

$$u(y) = -\frac{\varepsilon_0\varepsilon_f\zeta}{\mu}\mathbf{E}_x\left[1 - \frac{\psi(y)}{\zeta}\right]. \tag{15}$$

When $\psi(y) = 0$, the EOF velocity is given by the following Helmholtz-Smoluchowski equation:

$$u_{eof} = -\frac{\varepsilon_0\varepsilon_f\zeta}{\mu}\mathbf{E}_x. \tag{16}$$

The EOF velocity depends strongly on the electric field. However, if the EDL thickness is very small compared with the channel height (i.e., $\lambda_d \ll h$), the fluid flow has the form of a plug flow. In other words, the liquid is driven principally by the high shear force, which originates from the electrostatic force and acts only in the EDL region. However, as the EDL thickness approaches the channel height ($\lambda_d \approx h$), the flow profile changes from a plug-like profile to a nearly parabolic profile, since both the shear force and the electroosmotic driving force are reduced.

2.3 Electrical Conductance/Permselectivity

The conductivity (λ_i) of the electrolyte in a nanochannel is given by

$$\lambda_i = F^2 \sum_i z_i^2 v_i c_i = \sum_i \Lambda_i c_i, \tag{17}$$

where v_i is the mobility and $\Lambda_i = z_i^2 F^2 D_i/RT$ is the molar conductivity. The conductance effect in the nanochannel is determined jointly by the bulk ion concentration and the surface charge density. For a high ion concentration, the nanochannel conductance can be approximated using Eq. (17). However, for a low ion concentration, the conductance of the nanochannel is dominated by the surface charge since the counter-ions must balance the surface charge (i.e., $c_e = |\sigma_s|/hz_+F$). Thus, given the assumption of a symmetrical electrolyte, the nanochannel conductance is given as

$$K_n = \frac{2wh}{l}c_i^\infty(\Lambda_+ + \Lambda_-) + \frac{2w}{l}\frac{|\sigma_s|}{zF}\Lambda_+. \tag{18}$$

When the ratio of the channel height to the Debye length (i.e., h/λ_D) is less than 1, the fraction of K_n that is governed by the surface charge is given by the dimensionless Dukhin number. However, when the bulk concentration is higher than the concentration of the counter-ions, the electrical conductance is determined by both the bulk concentration and the channel geometry (i.e., the first term in Eq. (18)). When the concentration of the counter-ions in the nanochannel is larger than the bulk ion concentration, the total electrical conductance is dominated by the surface charge density (i.e., the second term in Eq. (18)). That is, the electrical conductance is only weakly related to the bulk concentration (i.e., the Dukhin number increases with a decreasing electrolyte concentration[34,36]). Finally, for the case where the first and second terms in Eq. (18) are equal, the electrical conductance saturates at a constant value, as shown in Figure 3.

© 2014 Wiley-VCH Verlag GmbH & Co. KGaA, Weinheim

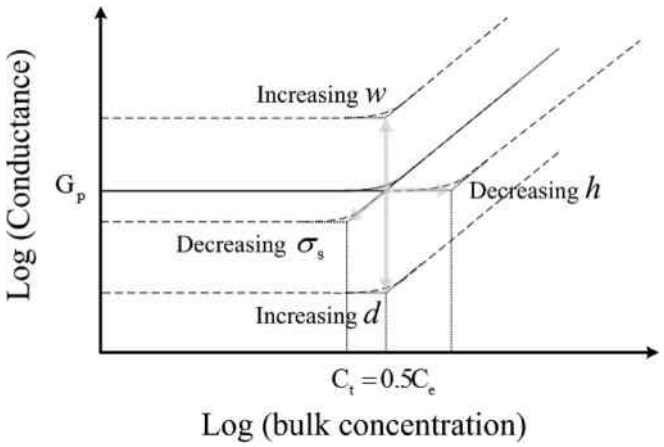

Figure 3. Electrical conductance of nanochannel as function of bulk concentration given different geometry and electrical properties.[3]

The term "permselectivity" is used to describe the situation where the nanochannel effectively selects the counter-ions to transport along the channel via the EDL and the external driving force. From the point of view of the Dukhin number, when $Du \gg 1$, the net charge density is much larger than the bulk ion concentration. Thus, the co-ions have only a negligible effect on the electrokinetic properties of cation-selective nanochannels, since $c_+ \gg c_-$. Recently, many researchers have exploited this phenomenon to perform desalination using ion exchange membranes.[37]

2.4 Streaming Current/Potential

When the aqueous solution is passed through the charged channel under the effects of a hydrostatic pressure difference, the counter-ions in the diffuse layer are transported in the downstream direction and induce an electric current, known as the streaming current, in the flow direction. The resulting streaming potential difference between the two ends of the channel produces an electric current, called the conduction current, in the opposite direction to the streaming current.[38–40] The feasibility for harvesting power (either mechanical or electrical) via the electrokinetic energy conversion (EKEC) process within nanoscale fluidic confinements has attracted significant attention in the literature. Recently, the streaming current and streaming potential have been widely employed in the application of microfluidic and nanofluidic devices, including flow rate meters,[41] pressure sensors,[42] zeta potential measurements,[43] and electrokinetic batteries.[15]

2.5 Electroviscous Effect

The electroviscous effect in narrow channels depends strongly on the surface potential, which depends, in turn, on the interactions between the properties of the substrate material and those of the bulk solution. The electroviscous effect in heterogeneous microchannels has been extensively examined using both analytical[35,44] and experimental[45,46] techniques. For pressure-driven flow in a nanochannel, the streaming potential generates both an electric current (i.e., the conduction current) and a liquid flow (i.e., electroosmotic flow) in the direction opposite to that of the pressure drop. The net result is a reduction in the flow rate in the pressure drop direction. This flow retardation phenomenon is conventionally referred to as the electroviscous effect.

For fluid flow on a surface with a no-slip condition, a previous study indicates the apparent viscosity reaches a maximum value in the mesoscopic regime, where the channel height is comparable with the Debye length, and the electroviscosity contribution to the apparent viscosity is below the 1 % level.[47] Recently, we presented a systematic study of electroviscosity effects in the nanofluidic channels using a triple layer model and a numerical framework. It was shown that the electroviscosity increases with an increasing pH value of the electrolyte solution and a decreasing ion concentration. For a very high ionic concentration, a smaller channel height leads to a higher electroviscosity. When the bulk concentration reduces from 10^{-3} M to 10^{-6} M, there is a critical channel height that maximizes the electroviscosity for a given a ionic concentration, and the critical channel height increases with the decreasing bulk concentration, as shown in Figure 4.[24]

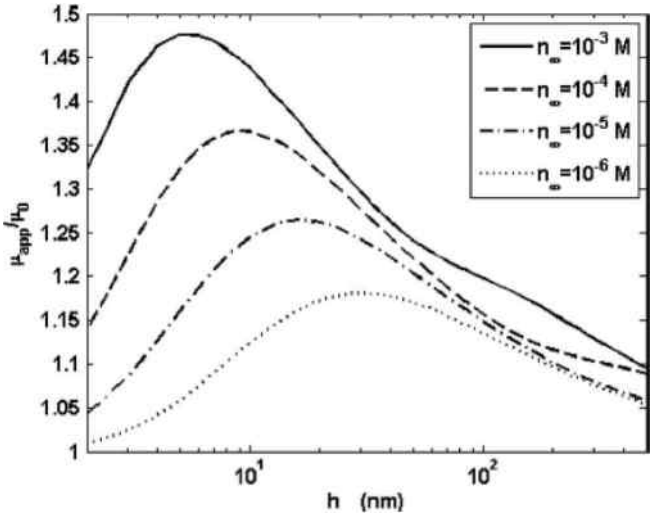

Figure 4. Electroviscosity effect as a function of the channel height for four different bulk concentrations.[24]

Further, we use the proposed overlapped EDL analytical model in an investigation performed to evaluate the effects of hydrodynamic slippage on the flow retardation caused by electroviscosity in nanochannels or nanotubes. As shown in Figure 5, it is shown that in the absence of slip, the maximum electroviscosity in nanochannels and

© 2014 Wiley-VCH Verlag GmbH & Co. KGaA, Weinheim

Israel Journal of Chemistry

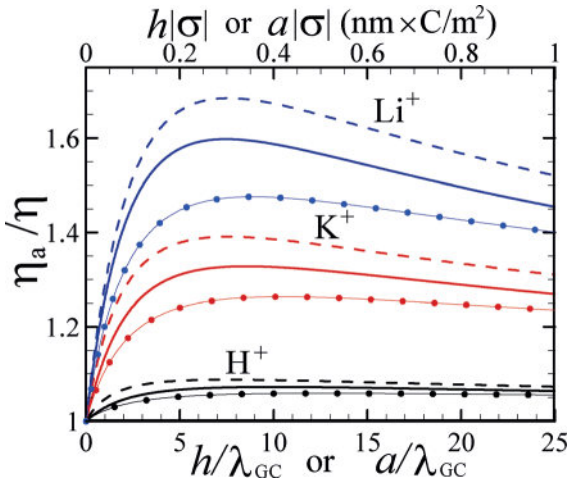

Figure 5. Electroviscosity in non-slip cation-selective nanochannels/nanotubes as function of h/λ_{GC} or a/λ_{GC}. Note that the bold, solid lines represent the results obtained for a nanochannel, while the dashed lines represent the approximate results for a nanochannel. Moreover, the lines with circle symbols represent the results obtained for a nanotube. The numerical results were obtained using the full PB model and given Cl^- co-ions, a low salt concentration of $c_i^\infty = 0.1$ mM, and a specific surface charge density of $\sigma = -10$ mC/m^2.[48]

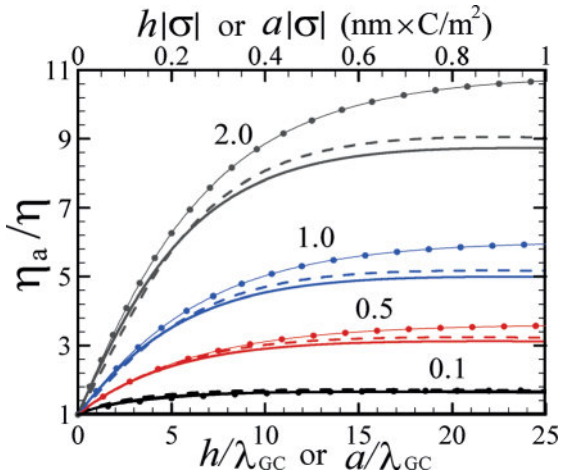

Figure 6. Electroviscosity in slip K^+ ion-selective nanochannels/nanotubes as function of h/λ_{GC} or a/λ_{GC}. Note that the bold, solid lines represent the results obtained for a nanochannel, while the dashed lines represent the approximate results for a nanochannel. Moreover, the lines with circle symbols represent the results obtained for a nanotube. The numerical results were obtained using the full PB model and given Cl^- co-ions, a low salt concentration of $c_i^\infty = 0.1$ mM, and a specific surface charge density of $\sigma = -10$ mC/m^2. The numbers in the figure represent the value of the slip ratio, i.e., b/h or b/a.[48]

nanotubes containing a unipolar solution of simple monovalent counter-ions occurs at surface charge densities of $h|\sigma| = 0.32\ \text{nm} \times \text{C/m}^2$ and $a|\sigma| \approx 0.4\ \text{nm} \times \text{C/m}^2$, respectively, where σ is the surface charge density. In addition, it is shown that the electroviscosity in the nanotube is smaller than that in the nanochannel. For example, given a LiCl solution, the maximum electroviscosites in a non-slip nanochannel and non-slip nanotube are $\eta_a/\eta \approx 1.6$ and 1.47, respectively. However, taking slip condition into account, the electroviscosity is greatly increased for both nanospaces. Significantly, the electroviscosity in the nanotube is greater than that in the nanochannel under slip conditions, as shown in Figure 6. When the slip length is comparable with the nanochannel half-height or nanotube radius, the electroviscous effect increases the intrinsic viscosity by more than 100 %.[48]

3 Continuum and Molecular Modeling

Three models, namely, the continuum, the mesoscopic, and the molecular models, are introduced for ion transport in nanochannels. Generally, the continuum model can be used when the geometric length scale is greater than 1 nm (equivalent to the thickness of approximately three water molecule layers); fluid flow obeys the continuum assumption and can therefore be described using the Navier-Stokes equation. For conservative approach, Daiguji[6] suggested the scale is ~5 nm instead of 1 nm. The molecular dynamics (MD) simulation is necessary to account for the behavior of molecules below this length scale. The MD provides a detailed field of interest. However, it is known that the time scale for an ion to cross a channel is much larger than the typical time scale of MD simulations. The conductance of the channel would not be evaluated by the MD simulations. The mesoscopic modeling, therefore, provides an alternative method for the simulations. Among the three models, the continuum approach provides the macroscopic transport phenomena quickly. The MD model provides the most detailed information, yet it requires extensive computational effort. The mesoscopic model can be a link between the continuum and MD models.

3.1 Continuum Modeling: Ion Transport

Mathematical models of the electrokinetic transport phenomenon generally impose the following conditions and assumptions: (i) the system is in a state of chemical and dynamic equilibrium; (ii) the transport process is in a steady state condition; (iii) the pore size is much larger than the liquid solvent molecule size; (iv) the ions in the Stern layer are rigidly attached to the surface and make no contribution to the bulk ionic current; (v) the flow is sufficiently slow that the ion convection effect can be ignored; (vi) the bulk ionic concentration is neither too high ($<1\ \text{mol l}^{-1}$) nor too low (the Debye length is less than ten times the channel width) and hence, the Poisson-Boltzmann model can be applied;[49] and (vii) no chemical reactions take place at the charged surface other than those associated with chemical adsorption or dissociation.

 © 2014 Wiley-VCH Verlag GmbH & Co. KGaA, Weinheim

3.1.1 Nernst-Planck Equation

Consider an N-component Newtonian electrolyte flowing with velocity $\mathbf{u}(\mathbf{r},t)$ in a microchannel with no polarization or chemical reactions. Let $\psi(\mathbf{r},t)$ be the electric potential prevailing within the solution, where $\mathbf{r}$ is the position vector. Furthermore, let the flux $\mathbf{J}_i$ of the ith ion species within the solute be given by the following constitutive equation:

$$\mathbf{J}_i = -\frac{\Lambda_i c_i}{z_i F}\nabla\psi - D_i\nabla c_i + c_i\mathbf{u}, \tag{19}$$

where c_i is the molar concentration of the ith ion species, z_i is the ith ion algebraic valence, F is the Faraday constant, D_i is the ion diffusivity. The flux contributions are due to electromigration in the electric field, concentration difference, and bulk convection, respectively. The ionic flux $\mathbf{J}_i$ and concentration c_i are related as

$$\frac{\partial c_i}{\partial t} + \nabla\cdot\mathbf{J}_i = 0. \tag{20}$$

The motion of the ion species produces an electric current density, $\mathbf{i} = F\sum_i z_i\mathbf{J}_i$, equal to

$$\mathbf{i} = -\nabla\psi\sum_i \frac{z_i^2F^2}{RT}D_i c_i - F\sum_i z_i D_i\nabla c_i + F\sum_i z_i c_i\mathbf{u}. \tag{21}$$

As shown in Eq. (21), the current is produced by the electric field, the concentration gradient, and the convection of the ion species. The electric current through the micro/nanochannel is thus calculated as $\mathbf{I} = \int_A \mathbf{i}dA = Fz\int_A(\mathbf{J}_+ - \mathbf{J}_-)dA$, where A is the cross-sectional area of the channel.

The continuum model, consisting of the Nernst-Planck equation, the Navier-Stokes equations, and the Poisson-Boltzmann equations, has been used to investigate many nanofluidic applications; for example, energy conversion, current control, sample preconcentration, and water purification. These will be illustrated in later sections.

3.2 Continuum Modeling: Motion of fluid

3.2.1 Navier-Stokes Equation

For an incompressible laminar flow, the fluid movement is governed by the continuity and the Navier-Stokes equations. For the flow in nanochannels, the Reynolds number (Re) is usually $\mathrm{Re}\ll 1$. The governing equations can be reduced to the following Stokes equations, i.e.,

$$\nabla\cdot\mathbf{u} = 0, \tag{22}$$

$$\rho\frac{\partial\mathbf{u}}{\partial t} = -\nabla p + \eta\nabla^2\mathbf{u} + \mathbf{F}, \tag{23}$$

where ρ is the fluid density, p is the applied external pressure force, and η is the dynamic fluid viscosity. Moreover, $\mathbf{F}$ can be any kind of body force, but is assumed here to be an electrical driving force. In general, this electrical driving force includes the Lorentz force induced by the external electric field, the force caused by electromagnetic susceptibility, and the intermolecular electric attraction. For the case of quasi-steady-state electrokinetic flow in a micro/nanochannel, the electromagnetic forces are negligible compared with the electrostatic force. Consequently, the driving force can be simplified as

$$\mathbf{F} = \rho_e\mathbf{E}, \tag{24}$$

where ρ_e is the net charge density and $\mathbf{E}$ is the electric field strength vector. Note that the net charge density ρ_e is expressed as

$$\rho_e = F\sum_i z_i c_i. \tag{25}$$

3.2.2 Hydrodynamic Slippage

In general, the surface properties of a material can be classified as either hydrophobic or hydrophilic. For fluid flow through a nanochannel, it is traditionally assumed that a no-slip condition exists at the boundary (see Figure 7). However, recent studies have shown that liquid slip occurs on bare (atomically smooth) surfaces and structure surfaces as a result of either molecular (intrinsic) slip or apparent (effective) slip.[27] Accordingly, Navier proposed a general boundary condition featuring a finite slip velocity whose magnitude varies linearly with the shear rate, i.e., $u_s = b(du/dy)|_{\mathrm{wall}}$. In general, the slip length is given as $b = \eta/\lambda$, where η is the fluid viscosity

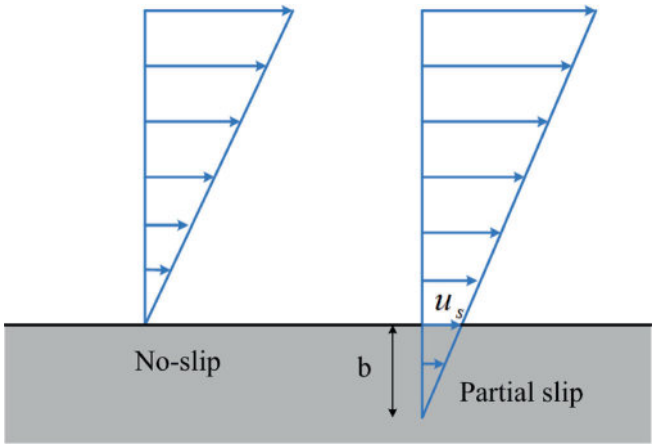

Figure 7. Schematic of the slip phenomenon at a liquid-solid interface.[26]

© 2014 Wiley-VCH Verlag GmbH & Co. KGaA, Weinheim

and λ is the friction coefficient. Notably, the slip length and the friction coefficient both depend strongly on the strength of the liquid-solid interaction. For a hydrophilic surface, i.e., a "wetting" surface with a very low contact angle (strong liquid-solid interaction), the slip length is usually smaller than the molecular dimensions, and thus, the flow at the solid-liquid interface can be described by the "no-slip" boundary condition. Huang *et al.*[50] reported that the slip length and contact angle are related by $b \propto (1+\cos\theta_c)^{-2}$. Meanwhile, Rothstein[26] showed that superhydrophobic surfaces enhance the mobility of droplets by reducing the contact angle hysteresis and lowering the frictional force between the fluid and the surface.

3.3 Mesoscopic Modeling

The continuity and momentum equations can be solved by tracking the movements of the molecule ensembles through the evolution of the distribution function,[51] using the well-known lattice Boltzmann equation (LBE). For flow with an external driving force, $\mathbf{F}$, the continuous Boltzmann-BGK equation has the form

$$\frac{Df}{Dt} \equiv \partial_t f + (\xi \cdot \nabla) f = -\frac{f - f^{eq}}{\tau_v} + \mathbf{F}, \tag{26}$$

where $f \equiv f(x,\xi,t)$ is the single particle distribution function in the phase space (x,ξ), ξ is the microscopic velocity, τ_v is the relaxation time, and f^{eq} is the Maxwell-Boltzmann equilibrium distribution. For a steady fluid immersed in a conservative force field, the equilibrium distribution function is defined by adding a Boltzmann factor to the Maxwell-Boltzmann distribution, i.e.,

$$f^{eq} = \frac{\rho_0}{(2\pi RT)^{D/2}} \exp\left(-\frac{U}{kT}\right) \exp\left(-\frac{(\xi - \mathbf{u})^2}{2RT}\right), \tag{27}$$

where U is the potential energy of the conservative force field, ρ_0 is the fluid density associated with minimum U, R is the ideal gas constant, D is the dimension of the calculation space, k is the Boltzmann constant, and $\mathbf{u}$ is the macroscopic velocity. A dimensional analysis gives the form of $\mathbf{F}$ as

$$\mathbf{F} = \frac{\mathbf{G} \cdot (\xi - \mathbf{u})}{RT} f^{eq}, \tag{28}$$

where $\mathbf{G}$ is the external force per unit mass.[51] It is noted that the Boltzmann-BGK equation given in Eq. (26) can be transformed into the continuum Navier-Stokes equation using the Chapman-Enskog expansion.

For the two-dimensional case, the third-order Gauss-Hermite quadrature formulation gives the nine-speed LBE model with discrete velocities as

$$\mathbf{e}_\alpha = \begin{cases} (0,0) & \alpha = 0 \\ (\cos\theta_\alpha, \sin\theta_\alpha)c, & \theta_\alpha = (\alpha-1)\pi/2 \quad \alpha = 1,2,3,4 \\ \sqrt{2}(\cos\theta_\alpha, \sin\theta_\alpha)c, & \theta_\alpha = (\alpha-5)\pi/2 + \pi/4 \quad \alpha = 5,6,7,8 \end{cases}, \tag{29}$$

where c is the speed of sound. Moreover, the density equilibrium distribution is given as

$$f_\alpha^{eq} = \omega_\alpha \rho_0 \exp\left(-\frac{U}{kT}\right)\left[1 + 3\frac{\mathbf{e}_\alpha \cdot \mathbf{u}}{c^2} + 9\frac{(\mathbf{e}_\alpha \cdot \mathbf{u})^2}{2c^4} - \frac{3\mathbf{u}^2}{2c^2}\right], \tag{30}$$

with

$$\omega_\alpha = \begin{cases} 4/9 & \alpha = 0 \\ 1/9 & \alpha = 1,2,3,4 \\ 1/36 & \alpha = 5,6,7,8 \end{cases}. \tag{31}$$

Thus, the discrete density distribution satisfies the following evolution equation:

$$f_\alpha(\mathbf{r} + \mathbf{e}_\alpha \delta_t, t + \delta_t) - f_\alpha(\boldsymbol{r}, t) = -\frac{1}{\tau_v}\left[f_\alpha(\boldsymbol{r}, t) - f_\alpha^{eq}(\boldsymbol{r}, t)\right] + \delta_t \mathbf{F}_\alpha, \tag{32}$$

where $\mathbf{r}$ is the position vector, δ_t is the time step, and τ_v is the dimensionless relaxation time and varies as a function of the fluid viscosity as follows:

$$\tau_v = 3\nu\frac{\delta_t}{\delta_x^2} + 0.5, \tag{33}$$

where ν is the kinetic viscosity and δ_x is the lattice constant (or grid size).

For electrokinetic flow in a dilute electrolyte solution, the external electric force given in Eq. (24) can be simplified as

$$\mathbf{F}_E = \rho_e \mathbf{E} - \rho_e \nabla \Phi, \tag{34}$$

where Φ is the stream electric potential caused by ion movements in the solution, based on Nernst-Planck theory. Generally, the stream potential dominates the electroviscosity effect in pressure-driven flow. However, in electrically-driven flow, its value is much less than the external potential and can be ignored. Therefore, the external force in the discrete LBE formulation should include both the pressure force and the electric force, i.e.,

$$\mathbf{F}_\alpha = \frac{(-\nabla P + \rho_e \mathbf{E} - \rho_e \nabla \Phi) \cdot (\mathbf{e}_\alpha - \mathbf{u})}{\rho RT} f_\alpha^{eq} \tag{35}$$

© 2014 Wiley-VCH Verlag GmbH & Co. KGaA, Weinheim

in which the macroscopic density and velocity are given respectively as

$$\rho = \sum_{\alpha} f_{\alpha} \quad \text{and} \quad \rho \mathbf{u} = \sum_{\alpha} \mathbf{e}_{\alpha} f_{\alpha}. \tag{36}$$

The potential distribution can be rewritten in the form of a Boltzmann-like equation by expanding the time-dependent term as

$$\frac{\partial \psi}{\partial t} = \nabla^2 \psi + g_{rhs}(\mathbf{r}, \psi, t), \tag{37}$$

where $g_{rhs} = \frac{1}{\varepsilon \varepsilon_0} \sum_i z_i e n_{i,\infty} \exp\left(-\frac{z_i e}{k_b T} \psi\right)$ represents the negative term on the right hand side of the original Poisson-Boltzmann equation. The evolution equation for the electric potential on two-dimensional discrete lattices can then be written as

$$g_{\alpha}(\mathbf{r} + \Delta \mathbf{r}, t + \delta_{t,g}) - g_{\alpha}(\mathbf{r}, t) = -\frac{1}{\tau_g}\left[g_{\alpha}(\mathbf{r}, t) - g_{\alpha}^{eq}(\mathbf{r}, t)\right] + (1 - \frac{0.5}{\tau_g})\delta_{t,g}\omega_{\alpha} g_{rhs}, \tag{38}$$

where the equilibrium distribution of the electric potential evolution variable g is given as

$$g_{\alpha}^{eq} = \pi_{\alpha}\psi, \quad \text{with} \quad \pi_{\alpha} = \begin{cases} 0 & \alpha = 0 \\ 1/6 & \alpha = 1,2,3,4 \\ 1/12 & \alpha = 5,6,7,8 \end{cases}. \tag{39}$$

The time step in Eq. (38) is evaluated as

$$\delta_{t,g} = \frac{\delta_x}{c'}, \tag{40}$$

where c' is the pseudo sound of speed in the potential field. Moreover, the dimensionless relaxation time in Eq. (38) is given as

$$\tau_g = \frac{3\chi\delta_{t,g}}{2\delta_x^2} + 0.5, \tag{41}$$

where χ is defined as the potential diffusivity and is generally set to unity.

The mesoscopic evolution equations given in Eqs. (38–41) are consistent with the macroscopic nonlinear Poisson-Boltzmann equation given in Eq. (9). After evolving on the discrete lattices, the macroscopic electric potential can be obtained as

$$\psi = \sum_{\alpha} (g_{\alpha} + 0.5\delta_{t,g} g_{rhs} \omega_{\alpha}). \tag{42}$$

Although the electric potential evolution equations are in an unsteady form, only the steady-state result is realistic, since the electromagnetic susceptibility effect is not considered. Moreover, even though the lattice evolution method is not as efficient as a multi-grid solution for the nonlinear Poisson equation due to its long wavelength limit, it is more suitable for complex geometries and parallel computing.

The boundary condition implementation plays a critical role in determining the accuracy of numerical simulations. The conventional bounce-back rule is one of the most commonly applied methods for describing the velocity boundary condition at a solid-fluid interface, due to its simple implementation.[51] However, the bounce-back rule has two major disadvantages. First, it requires the dimensionless relaxation time to lie strictly within the range of 0.5–2.0, since otherwise, a prediction error inevitably occurs. Second, the non-slip boundary implemented using the conventional bounce-back rule is not precisely located at the boundary nodes, and thus an inconsistency arises when coupling with other PDE solvers on the same grid set.[52]

To overcome the inconsistence between the lattice Boltzmann method (LBM) and other PDE solvers on a same grid set, the boundary condition treatments of the PDE solver for the electric potential distribution must be modified in such a way that they are consistent with the LBM, bounded by the bounce-back rule. Accordingly, Zou and He[53] proposed a half-way bounce-back rule for non-equilibrium distributions, applicable to both hydrodynamic and electrodynamic boundary implementations.

At the solid-liquid interface, the following hydrodynamic boundary condition holds:

$$f_{\alpha}^{neq} = f_{\beta}^{neq}, \tag{43}$$

where subscripts α and β simply represent opposite directions. By analogy, the non-equilibrium bounce-back rule for the electric potential distribution at the wall surface can be expressed as

$$g_{\alpha}^{neq} = -g_{\beta}^{neq}. \tag{44}$$

The half-way bounce-back scheme with interpolation provides a convenient means to deal with curved surfaces.[54] In addition, the bounce-back scheme has a super-linear accuracy when the wall surface varies between two adjacent nodes, and an approximately second-order accuracy if the wall surface is located at the middle. Finally,

© 2014 Wiley-VCH Verlag GmbH & Co. KGaA, Weinheim

the half-way bounce-back method is easy to implement for complicated boundary conditions without any special considerations required to accommodate the corners.

3.4 Molecular Modeling

The major challenge in performing molecular dynamics simulations of the electrokinetic flow (EKF) phenomenon comes in dealing with the effects of the long-range Coulomb potential between the charged particles. Unlike the Lennard-Jones potential and other short-range potentials, the Coulomb interaction force cannot be truncated, and direct summation is computationally prohibitive for traditional EKF problems. As a result, significant effort has been expended in developing new algorithms for achieving a more efficient treatment of these long-range interactions.

The most widely used method for treating the Coulomb force is the Ewald summation method,[55] in which the total electrostatic potential is rewritten as a summation of three terms, namely a short-range term that is calculated in real space, a long-range term that is evaluated analytically in reciprocal space, and a constant self-interaction term. However, even with an optimized selection of the Ewald parameters, the computation time still scales as $N_p^{3/2}$, where N_p is the total number of particles. As a result, the Ewald method is unsuitable for the simulation of large systems. Accordingly, Darden *et al.*[56] presented the particle-mesh Ewald method, in which the long-range interactions were calculated using the fast Fourier transform technique on a mesh. It was shown that the computation time of the proposed method scaled as $N_G\log(N_G)$, where N_G is the number of mesh grid points. The fast multipole method has the potential to scale linearly with N_p. However, its implementation must be carefully designed to achieve this optimized scaling.

An efficient treatment of the long-range Coulomb forces between charges is essential in reducing the computation time of the simulation process. Accordingly, Beckers *et al.*[57] proposed a particle-particle particle-mesh (P3M) scheme of the form shown in Figure 8. Notably, while the figure shows a two-dimensional schematic of the P3 M scheme, the simulations are actually performed using a three-dimensional implementation. In the P3M method, the total force acting on each particle is divided into two components, namely a short-range force within a user-defined distance (e.g., within the circle shown in Figure 8) and a long-range force outside this distance. The short-range force comprises the Coulomb force and the van der Waals force and is treated precisely by the particle-particle (PP) method using a simple direct summation approach, while the long-range force is calculated using the particle-mesh (PM) method by solving the Poisson equation for the electric potential on the mesh. Notably, the P3M method combines the accuracy of the PP method with the efficiency of the PM method. Furthermore, by using a high-efficiency multi-grid approach to solve the Poisson equation in each time step, the computational cost reduces to just $O(N_G)$.

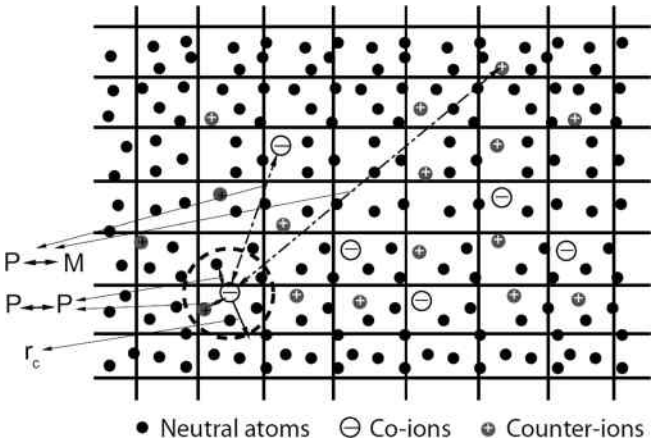

Figure 8. Two-dimensional representation of P3M algorithm. The mesh has spacings of h_x and h_y in the horizontal and vertical directions, respectively. The short-range contributions (P↔P) are obtained by direct summation over a region with radius r_c (dashed circle), while the long-range contributions (P↔M) are obtained using particle-mesh method.

In summary, in the P3M method, the total force acting on each particle comprises two parts: namely, the short-range forces exerted by nearby particles, F^{PP}, and the long-range forces obtained by solving the Poisson equation for the electric potential on a mesh, F^{PM}. The short-range force, F^{PP}, consists of two parts, i.e., the total van der Waals force exerted by the particles within the cut-off distance, F^{LJ}, and the total Coulomb force exerted by the particles within the Coulomb cut-off distance, F^{C}. Meanwhile, F^{C} also contains two parts, namely the direct Coulomb force exerted by other charged particles and a correction force due to double counting in the short and long-range calculations.

3.4.1 Benchmark

To verify the P3M scheme for long-range Coulomb interactions and the treatment of the boundary conditions for slab-like geometries, we calculate the Coulomb force between two particles with opposite charges. This is the most straightforward and accurate test of different treatments for the long-range force. Periodic boundary conditions are imposed in the x and y directions, respectively. The dimension in the z-direction is four times that of L_x. We first calculate forces assuming periodic boundary conditions along z and then subtract the effect of periodic images using the correction. The accuracy of the P3M approach can be improved by refining the mesh size or increasing the cutoff distance $r_{c,C}$, but this increases the computational cost.

© 2014 Wiley-VCH Verlag GmbH & Co. KGaA, Weinheim

Israel Journal of Chemistry

Figure 9 shows the Coulomb force as a function of the separation distance before (triangles) and after (squares) correcting for the periodic boundary condition in the z-direction. At small separation distances, both results approach the bare Coulomb force (solid line). However,

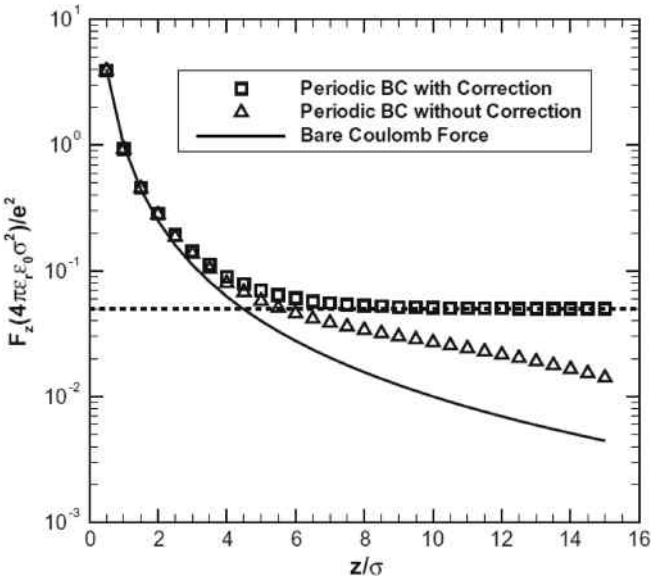

Figure 9. Coulomb force between two charges as function of separation distance. Numerical results before (triangles) and after (squares) correcting for periodic images along z are compared with bare Coulomb interaction (solid line) and analytic limit (dashed line) for large separations. Note that the domain size is given as $L_x = 10.43\sigma$, $L_y = 12.04\sigma$, and $L_z = 4L_x = 41.72\sigma$. Moreover, the mesh size is approximately 1σ and the Coulomb cutoff distance is $r_{c,C} = 8\sigma$.

when the separation distance is large compared with L_x and L_y, the interaction between the periodic images of the charges becomes equivalent to the interaction between two charged surfaces, and thus, the force approaches a constant value which can be calculated analytically. It is seen that following correction, the numerical results are in excellent agreement with the asymptotic result (dashed line). Merely increasing the empty space without applying the correction does not improve the accuracy of the results. However, when the correction process is included, an empty space of the order of the larger of L_x or L_y is sufficient to ensure the accuracy of the numerical results.

3.4.2 Electroosmotic Flow in Smooth Nanochannels

The molecular dynamics approach has been extensively used to investigate the transport laws and mechanisms associated with EOF in smooth nanochannels. Qiao and Aluru[58] modified the traditional PB equation by introducing an electrochemical potential correction extracted from the ion distribution computed for a small channel using MD simulations. It was shown that the results obtained by the modified PB equation for the ion distribution in channels with larger channel widths were in good agreement with the theoretical results.

In using MD simulations to clarify the applicability of continuum theories, such as the PB model in describing the EOF phenomenon at the nanoscale, the observers must stand on the same base to avoid definition gaps. For example, when presenting the MD results, the bin size should not be smaller than the solvent molecular diameter considered in continuum theory, since otherwise, the MD results are not the macroscopic properties at the same level of the continuum. Furthermore, the effect of the Stern layer must be carefully considered. The traditional PB equation describes only the ion distribution in the diffusion (i.e., outer) layer of the EDL.[59] In continuum theory, the compact (inner) layer of the EDL is too thin (molecular scale) to be considered, and thus the PB equation is used to describe the ion distribution over virtually the entire domain. However, in nanofluidics, the inner layer (i.e., the Stern layer) is comparable with the channel width in size, and thus both the Stern layer and the diffuse layer are considered in MD simulations. Therefore, in comparing the MD results with the PB predictions, the Stern layer must be excluded to ensure a fair comparison.[60]

Figure 10(a) shows the distribution profiles of the counter-ions and co-ions in a smooth, straight nanochannel. As shown, the extent of the Stern layer is given by the difference between the starting point of the counter-ions and that of the co-ions. Thus, we compared the MD results with the PB predictions in the whole channel or in the diffusion layers only. Figure 10(b) shows that while the MD results deviate notably from the PB predictions over the entire channel width, a good agreement exists between the two sets of results for the diffusion layer region of the channel.[60]

The Poisson-Boltzmann equation is based on a Boltzmann distribution of the ions within a dilute solution. The assumption of a dilute solution is reasonable in most macroscopic cases; however, it becomes somewhat critical for nanoscale electroosmosis applications. In practice, the extent to which the PB equation holds for such applications can be evaluated by progressively changing the number of ions in the solution and comparing the corresponding MD results with the PB predictions. The bulk ionic concentration can be determined by taking the average value of the MD results for the ion concentration in the equilibrium state at the centerline of the channel. Thus, the cases have a wide bulk ionic concentration range from 0.1 M to 5.25 M. Figures 10(c)–10(d) show that the Poisson-Boltzmann equation holds for low and moderate ionic concentrations. When the bulk ionic concentration is lower than 0.88 M, the PB predictions agree well with the MD results. However, as the ionic concentration increases, the deviation between the two sets of results increases. In other words, the Boltzmann distribu-

 © 2014 Wiley-VCH Verlag GmbH & Co. KGaA, Weinheim

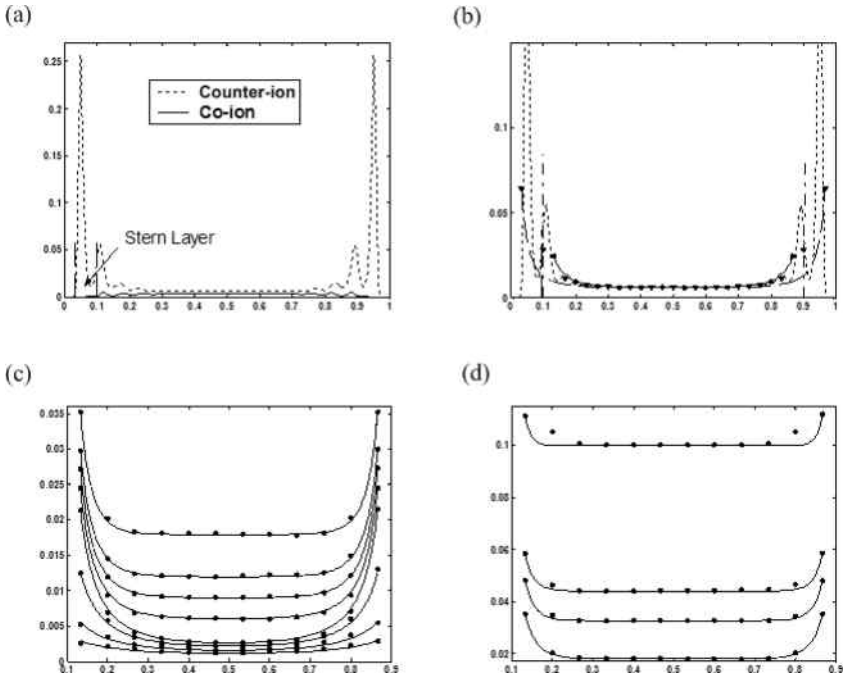

Figure 10. Comparison of MD simulation results and Poisson-Boltzmann results for ion distribution in a smooth, straight nanochannel. (a) Stern layer determination from MD results. (b) Dotted line shows MD results obtained using finest bin size, while circles and triangles denote results obtained using bin size equal to one molecular diameter. Triangles denote sampling over entire channel width, *W*, while circles denote sampling over the diffusion layer only. Dot-dash lines indicate interface between the Stern layer and the diffusion layer. Finally, the dashed line and the solid line were calculated based on the PB equation for different channel widths and zeta potentials. (c) Ionic density profiles from MD simulations and PB predictions for moderate and low ionic concentrations. (d) Ionic density profiles for high ionic concentrations. Ion density is normalized by $|e|/\sigma^3$, i.e., $\rho_e^* = \frac{\rho_e}{|e|/\sigma^3}$, and the z-position is normalized by the channel width, i.e., $z^* = \frac{z}{W}$.

tion breaks down, and thus, conventional Poisson-Boltzmann theory can no longer be applied to describe the electrokinetic transport behavior – see Figure 10(d).[60]

3.4.3 Electroosmotic Flow in Rough Nanochannels

The presence of regular or random surface roughness reduces the EOF flow rate dramatically, even though the roughness is very small compared with the channel width.[61] Figures 11(a) and 11(b) present schematics of nanochannels with two common roughness geometries, namely rectangular bumps and random hills, respectively. Figure 11(c) shows the variation of the dimensionless flow rate with the dimensionless channel height, given random roughness and rectangular bumps, respectively, and a constant surface charge density. The results show that random roughness leads to a more significant reduction in the flow rate than regular rectangular bumps. This result is consistent with previous studies, which showed that two bumps with half the width result in a more significant reduction in the flow rate than a single wide bump. The flow rate is actually similar to that observed for a two-bump case with the same mean height, even though the height changes much more frequently in the random roughness case. This finding suggests that local height changes that allow the fluid to flow around obstacles in the y-direction are less effective in blocking the flow than obstacles which extend along the y-direction.

4 Applications

4.1 Energy Conversion

In nanochannels, the surface charge causes the ions within the electrolyte to be redistributed, and thus, the EDL is formed in the solution near the charged surface.[62,63] As a result, when the electrolyte is driven through the channel, it causes a movement of the electric charges in the downstream direction. In practice, accumulating the charges at the channel ends represents an effective means of converting mechanical energy into electrical power, as shown in Figure 12(a). This process can be referred to as electrokinetic energy conversion in a generation electrical mode, indicating a conversion of hydrostatic energy into electrical power via electrokinetic phenomena. The power driving an external load is from the streaming current/potential, due to the presence of the electrical double layer in the liquid flow passage. Morrison and Osterle[64] predicted a maximum conversion efficiency of 0.9% when driving pure water through a glass capillary with a radius of about 100 nm. Similarly, Van der Heyden *et al.*[65] reported a maximum EKEC of 12%

© 2014 Wiley-VCH Verlag GmbH & Co. KGaA, Weinheim

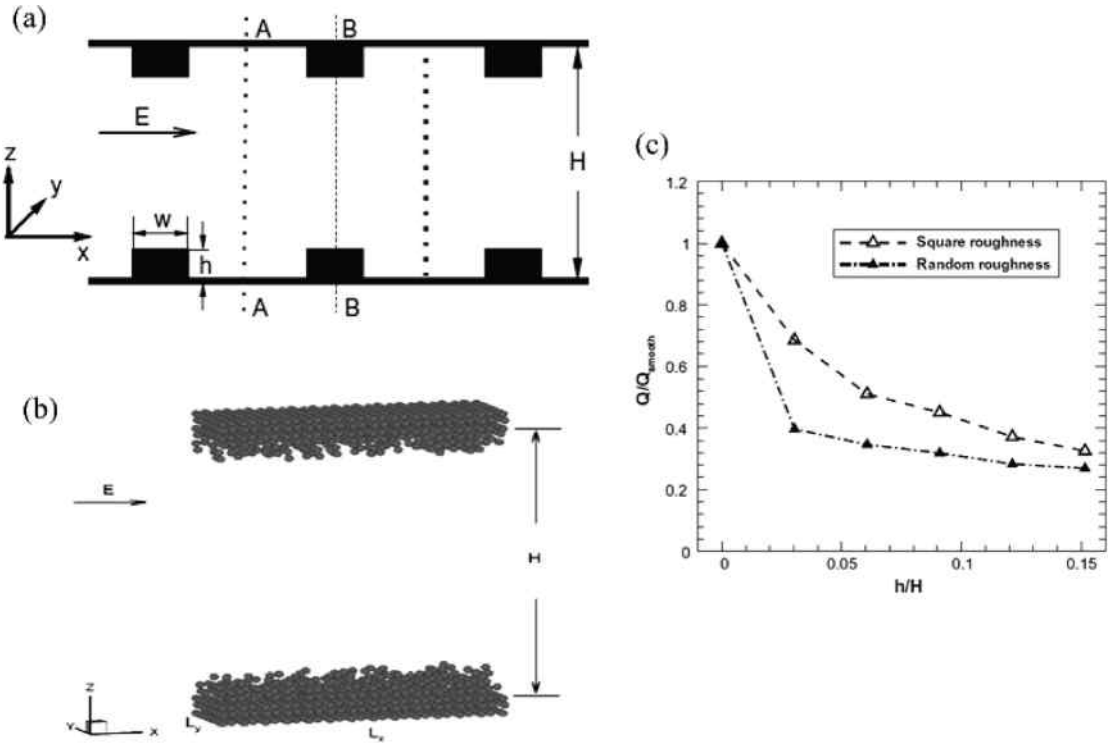

Figure 11. (a) Schematic of roughness in the form of rectangular bumps. (b) Schematic of roughness in the form of random hills. (c) Variation of flow rate with roughness height for regular bumps (open symbols) and random roughness (filled symbols). The regular bump covers half the surface $w = L_x/2$, and thus, the mean height of both surfaces is equal to h/2. The surface charge density is $-0.092e/\sigma^2$ in both cases, and the statistical errors are smaller than the symbol size.

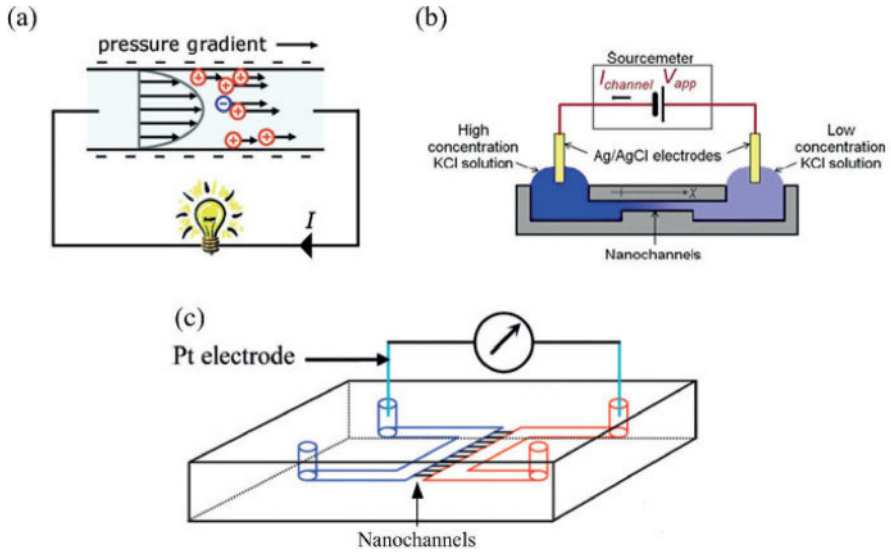

Figure 12. Schematics of three typical configurations for electrical energy generation using nanofluidics. (a) Energy conversion from mechanical to electrical power. (b) Electrical energy generation due to diffusion potential difference. (c) Electrical energy generation due to electrochemical reaction.[70,71,74]

when using LiCl electrolyte solution, but conversion efficiencies of 7% and 2% when using KCl electrolyte solution and pure water, respectively. Thus, it was inferred that the conversion efficiency is reduced with increasing mobility of the monovalent counter-ions in the aqueous solution. Chang and Yang[19] showed that the conversion efficiency is also reduced when the resistance of the nanochannel is less than that of the reservoirs at either end of

© 2014 Wiley-VCH Verlag GmbH & Co. KGaA, Weinheim

the channel, due to the formation of an ion depletion zone. However, previous studies have indicated the lower energy conversion efficiency is due to the fluid flow on the surface using a material with hydrophilic properties (no-slip boundary condition at the surface). In recent years, many researchers use the surface property of hydrophobic solutions (slip boundary condition at the surface) to improve the low energy conversion efficiency when in the generation mode of EKEC. Eijkel[66] showed that hydrodynamic slippage is beneficial in enhancing the electrokinetic energy conversion efficiency in micro- and nanochannels. Davidson and Xuan[67] showed that a maximum conversion efficiency of more than 30% is theoretically possible given a slip length of 5 nm. Ren and Stein[68] predicted a conversion efficiency of 40% given a nanochannel with a length of 10 nm and a slip length of 30 nm. Furthermore, a maximum conversion efficiency of more than 70% might be achieved with a slip length of 100 nm in a carbon nanotube filter.

The term "electrokinetic micro-battery", as shown in Figure 13, has been studied extensively. Taking hydrodynamic slippage into account, we derived an exact expression[15] for the figure of merit (Z), to evaluate the electrokinetic energy conversion efficiency and power of an ion-selective nanopore. An ion-selective nanopore usually refers to the situation when the counter-ions strongly dominate the ion transport of a nanopore, i.e., the Dukhin number ($Du = c_e/c_i^{\infty}$) is much larger than unity. The co-ions only have a negligible influence on the electrokinetic properties of a cation-selective nanopore due

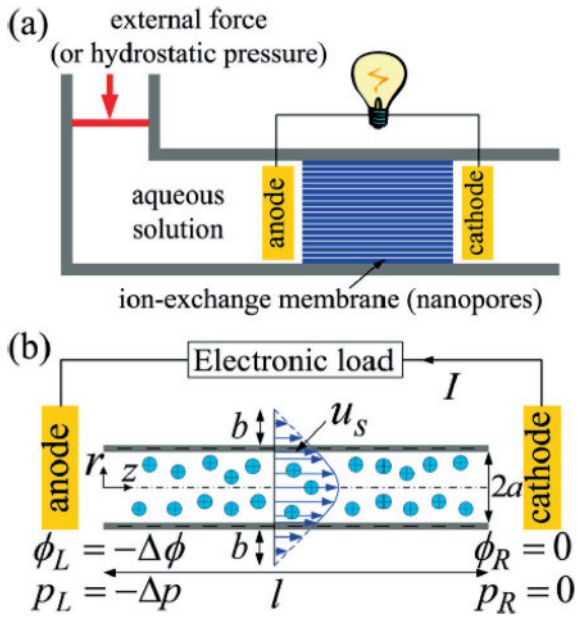

Figure 13. (a) A schematic of an electrokinetic battery. (b) A schematic of electrokinetic power generation in a cation-selective nanopore. *a* and *l* are the pore radius and length, respectively. Δp and $\Delta\phi$ are, respectively, the pressure difference and the potential difference. *b* refers to the slip length.[15]

to $c_+ \gg c_-$ inside the nanopore. As the result, the EDL potential and the counter-ion distribution inside the cation-selective nanopore are determined from the simplified Poisson-Boltzmann equation.[15]

In Figure 14, $a/\lambda_{GC} \ll 1$ (low-σ limit), implying that the counter-ions have a more uniform distribution inside a nanopore. Streaming conductance (S_{str}) and electrical conductance (K_n) are both linearly proportional to $|\sigma|$. The streaming conductance is scaled with $S_{str} \propto a/\lambda_{GC}$, where *a* is the pore radius. The electrical conductance contributed by electroosmosis is negligible, due to

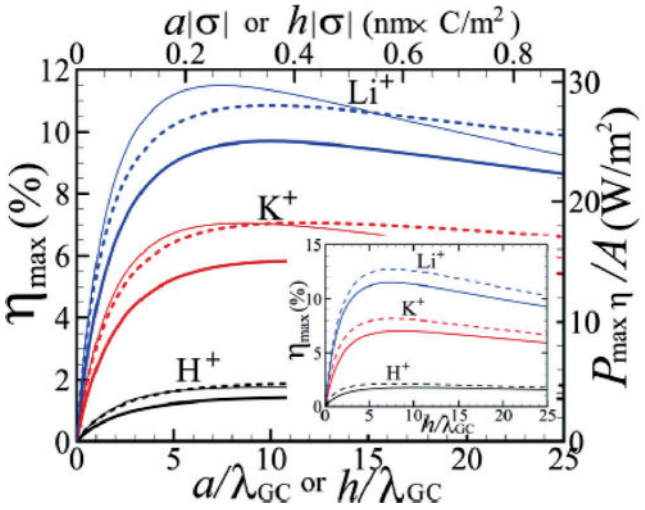

Figure 14. Plots of the maximum conversion efficiency (η_{max}, bold solid line) and the corresponding output power density ($P_{max\eta}/A$, dashed-line) of a cation-selective nanopore as a function of a/λ_{GC} in the absence of slip.[15]

a lower value of $|\sigma|$, indicating a smaller EOF velocity. The electrical conductance is dominated by ionic electromigration, and can be scaled with $K_n \propto \Gamma a/\lambda_{GC}$, where the $\Gamma = \mu z_+ F m_+ / 2\varepsilon_0\varepsilon_f RT$ is the ratio of electromigration and electroosmosis, μ is the fluid viscosity, and m_+ is the counter-ion mobility. Further, the figure of merit is reduced to $Z = a/4\lambda_{GC}\Gamma$. Since a low-$\sigma$ regime has a small value of Z, the efficiency is approximately $\eta_{max} \approx Z/4$. Then, we have an approximation of the efficiency of a nanopore: $\eta_{max} \approx a|\sigma|/16\mu m_+$. While $a/\lambda_{GC} \gg 1$ implies that most counter-ions are located within a thinner layer near the walls, due to the lower flow velocity near the walls, it slightly increases with $|\sigma|$ and it has a scaling law of $S_{str} \propto \ln[(a/\lambda_{GC})/2e]$. EOF contribution to the electrical conductance becomes considerable, due to a larger value of $|\sigma|$ yielding a larger EOF velocity, i.e., $K_n \propto (1+\Gamma)a/\lambda_{GC}$. Thus, $Z = (\ln|\sigma|)^2/(1+\Gamma)|\sigma|$, and this is why η_{max} and $P_{max\eta}$, which are shown in Figure 14, both decrease very slightly in a high-$a|\sigma|$ regime. The highest power densities of H^+, K^+, and Li^+ in a 50 nm nanopore with $\sigma \approx -7$ mC/m² are estimated to be 4.8, 18, and 28 W/m², respectively. In the absence of slip, and when the ratio of

© 2014 Wiley-VCH Verlag GmbH & Co. KGaA, Weinheim

the radius and the Gouy-Chapmann length (a/λ_{GC}) is approximately 10, the highest efficiency for an electrolyte consisting of simple monovalent ions was predicted to be approximately 9.7%. While this efficiency is low, it can be greatly improved to a potentially practical efficiency (>40%) when the slip ratio (b/a) is greater than 0.7.

Figure 12(b) shows an alternative configuration for generating electrical energy from ion transport by means of a nanochannel connecting two reservoirs containing electrolyte solutions with different concentrations. Since the channel surfaces are charged, the counter-ions are transported through the nanochannels more readily than the co-ions, and thus a net charge migration occurs. The Gibbs free energy of mixing, which forces ion diffusion, can thus be converted into electrical energy by using ion-selective nanochannels. This energy conversion process is conventionally referred to as reverse electrodialysis (RED). The concept of RED for energy generation was presented as early as 1954;[69] however, these applications have attracted renewed interest in recent decades due to rapid advancements in the microfluidics and nanofluidics fields.[70,71] In general, such applications are characterized by the need for a high energy-conversion efficiency and a high output power. Thus, efficient mechanisms for modeling the electro-chemical-mechanical energy conversion process are urgently required. Recently, we presented the numerical simulations examining the effect of salt concentration gradient direction on RED performance in negatively-charge conical nanopores, as shown in Figure 15. Compared with the cylindrical nanopore,[72] the conical-shaped nanopore showed a dependence on the direction of the salt concentration gradient on RED performance. When ion diffusion is from the base side to the tip side, the transference number of counter-ion is larger than for the diffusion from tip to base. This is due to an addition in the EDL overlap near the tip side. In general, a larger transference number indicates a higher conversion efficiency. In other words, RED in conical nanopores shows a better performance when the concentration gradient is from the base side to the tip side.[73]

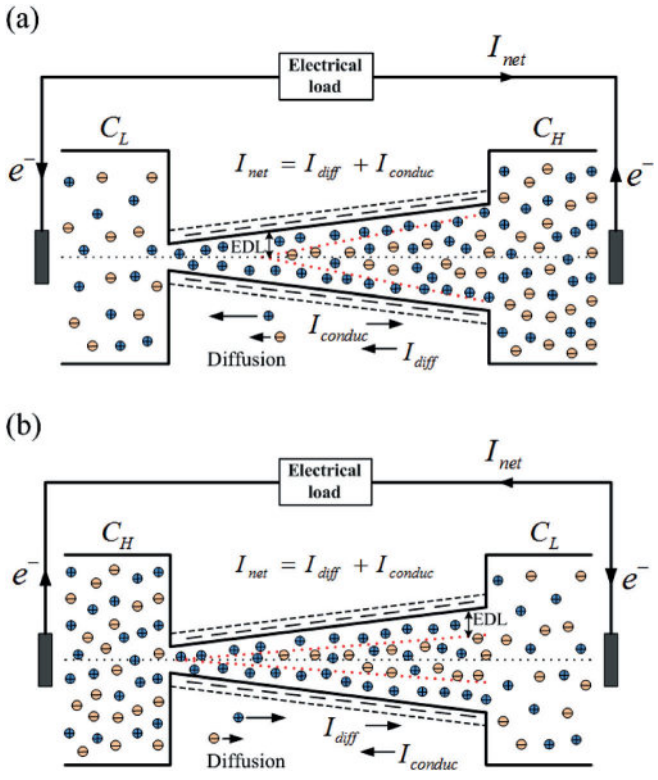

Figure 15. Schematic of power generation in negatively-charged nanopore as a result of reverse electrodialysis. (a) Ion diffusion through the nanopore from the base side to the tip side under the effects of concentration gradient. (b) Ion diffusion through the nanopore from the tip side to the base side under the effects of concentration gradient. Due to the geometrical effect and different concentration gradient, a different degree of electrical double layer overlap occurs between the walls of the nanopore in the two cases.[73]

Figure 12(c) shows an alternative means of acquiring electrical energy from ion transport, using an array of parallel nanochannels connecting two microchannels filled with fuel and oxidant, respectively. In such a system, the energy is harvested by the electrochemical reactions which take place following proton exchange through the ion-selective nanochannels (i.e., an oxidation reaction at the anode side and a reduction reaction at the cathode side). Previous studies have shown that the proton conductivity in the nanochannel (and thus the electrical performance of the nanofluidic fuel cell) can be enhanced by establishing an EDL within the channel, since under this condition, proton transport is dominated by the surface charge.[74]

4.2 Electric Current Control: Ion and Molecule Transport

When the Debye length is comparable with the characteristic scale of the nanochannel, a non-electroneutral state exists in the channel. In other words, the concentration of the counter-ions is greater than that of the co-ions. When the EDL is strongly overlapped (i.e., $\lambda_d \gg h$), the concentration of counter-ions is much larger than that of the co-ions ($c_+ \gg c_-$), and thus an ion-selective nanochannel is produced. Notably, this phenomenon can be exploited to separate the ions or charged molecules in the channel, by means of the so-called exclusion-enrichment effect.

Given the existence of an EDL overlap, the concentration of the mobile counter-ions in the nanochannel is higher than the bulk concentration (i.e., $Du \gg 1$), and thus ion or molecular conduction in the nanochannel is dominated by the surface charge density. As a result, the ions or molecules in the nanochannel can be easily controlled and transported by the EEE. In recent years, many researchers have exploited the EEE to develop nanofluidic electronic devices, such as diodes and field-effect transistors. As shown in Figure 16, existing nanofluidic diodes

© 2014 Wiley-VCH Verlag GmbH & Co. KGaA, Weinheim

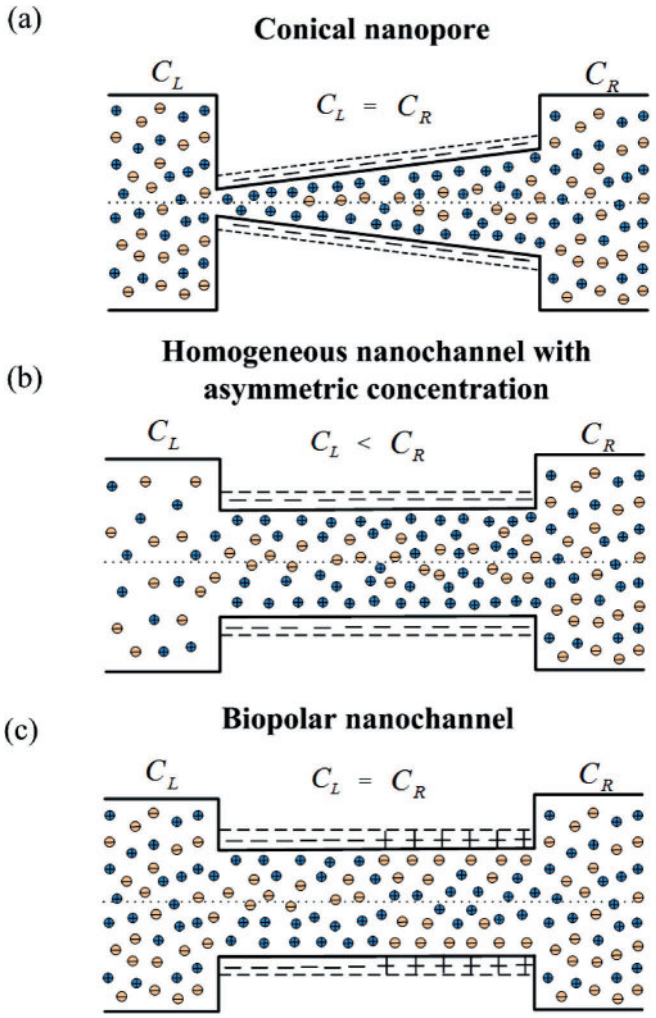

Figure 16. Ionic rectification effect in three different types of nanofluidic device in the equilibrium state. The ionic rectification effect under forward and reverse bias is discussed in Ref. [17].

can be categorized into three main types. The first type comprises a conical-shaped nanochannel, the second type contains a uniform nanochannel connecting two reservoirs containing electrolyte solutions with different concentrations, and the third type is analogous to the III-V compound semiconductor (in which the bipolar nanochannel plays the part of the P-N junction).[6,17] As shown in Figure 17, when a forward bias is applied, an ion enrichment region is formed near the bipolar interface in the nanochannel. Conversely, when a reverse bias is applied, an ion depletion region is formed. The electrical resistance of the nanochannel with the application of a forward bias is greater than that of the channel under a reverse bias, due to the higher ion concentration in the ion enrichment region, and consequently, a rectification effect is induced. The ionic rectification effect can be defined as the ratio of the electric current under a forward bias to that under a reverse bias (i.e., Rectifying factor = $|I(V_+)|/|I(V_-)|$).[75] Yusko *et al.*[76] showed that ion current

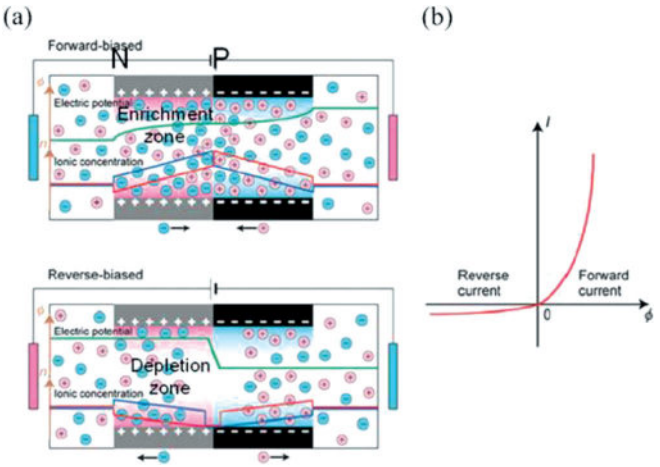

Figure 17. (a) Electric potential (along nanochannel), ionic concentration, and (b) typical I–V curve under forward bias and reverse bias. The surface charge in the left and right halves of the channel is constant and the bulk solution has a concentration of 5 mM.[75]

rectification in an electroosmotic diode is independent of the electrolyte concentration, providing that the pore size is at least 500 times larger than the Debye length. Moreover, Singh *et al.*[77] showed that the rectification effect in a bipolar channel increases with increasing junction sharpness due to an increasing unipolar characteristic of the electrolyte.

For field-effect control (i.e., electrostatic ionic gating) in nanofluidics, the basic concept is that of a nanofluidic transistor which is analogous to a metal-oxide-semiconductor field-effect transistor (MOSFET). The semiconductor field-effect transistor has been extensively studied for ion and molecular transport via surface charge modulation.[16,78] However, the concept of an electrostatic gate as a controller for the manipulation of ions or molecules in the EDL, by applying a voltage on the electrode that directly affects the arrangement of charges in the dielectric layer, is shown in Figure 18. The electrostatic relationship between solid (i.e., oxide) and liquid (i.e., EDL) is given by $\varepsilon_0\varepsilon_f d\phi/dy|_{wall} = \varepsilon_0\varepsilon_d d\phi/dy|_{wall}$, without considering the Stern layer, where ε_d is the permittivity of the oxide. The electric potential relation can be obtained from basic electrokinetic theory, which can be written as

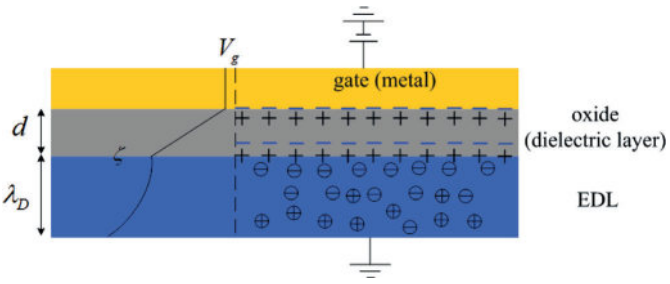

Figure 18. Schematic of an electrostatic gate.

© 2014 Wiley-VCH Verlag GmbH & Co. KGaA, Weinheim

$$V_g = \zeta + \frac{2\varepsilon_f RTd}{\varepsilon_d zF\lambda_d}\sinh\left(\frac{zF\zeta}{2RT}\right). \quad (45)$$

In general, electrostatic gates are designed for the overlapping EDL condition.[79,80] Further, Liu *et al.*[81] investigated the modulation for electrically-gated nanopores with non-overlapped EDL. The results indicated that the field-effect is extended far beyond the Debye length, resulting in a nonlinear current.

4.3 Sample Preconcentration

Various strategies have been proposed for achieving preconcentration in liquids, including field-amplified stacking,[82] isotachophoresis,[83] temperature gradient focusing,[84] and electrokinetic trapping.[85–87] Amongst these various techniques, electrokinetic trapping is particularly advantageous since it can be used for any charged molecule species. Preconcentration devices combine microscale and nanoscale channels, and feature a non-equilibrium condition near the micro-/nano-interface under an appropriate potential gradient. The nanochannel has an ion-selectivity characteristic given by $Du \gg 1$. In other words, the counter-ions dominate the ion transport within the nanochannel, even if the EDL does not overlap.[34] As a result, an ion electro-migration flux imbalance is produced between the microchannel and the nanochannel when an external electric field is applied. Moreover, a concentration gradient is induced near the micro/nanochannel interface which drives a diffusion flux to balance the ion flux of the microchannel-nanochannel system. In other words, the ions are depleted on the anodic side and enriched on the cathodic side of a negatively-charged nanochannel. As shown in Figure 19, when applying the external electric potential through the membrane, electroosmosis will be induced. The nanochannel acts as a cation-selective membrane. The anions migrate toward the anodic side of the nanochannel, generating a concentration polarization region near the end of the nanochannel. To maintain the electroneutrality condition near the anodic side of the nanochannel, the concentration of cations also reduces. As a result, the depletion zone is generated near the anodic side of the nanochannel. The complex physics associated with this ion concentration polarization effect cannot be adequately described using the equilibrium model of the EDL (i.e., the PB model). Rather, the diffusion, migration and convection effects should be examined using the Poisson-Nernst-Planck model.[16] In general, the ICP phenomenon is related to the current-voltage (I–V) curve of the nanochannel, which reflects the electrical properties of the channel and yields useful insights into the transport mechanism of the local ions. As shown in Figure 20, the classical I–V curve

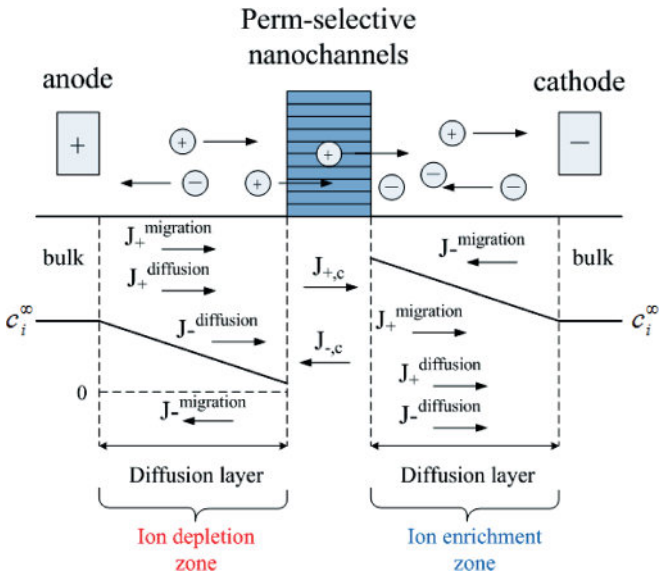

Figure 19. Interpretation of ion concentration polarization effect from a molar flux perspective.

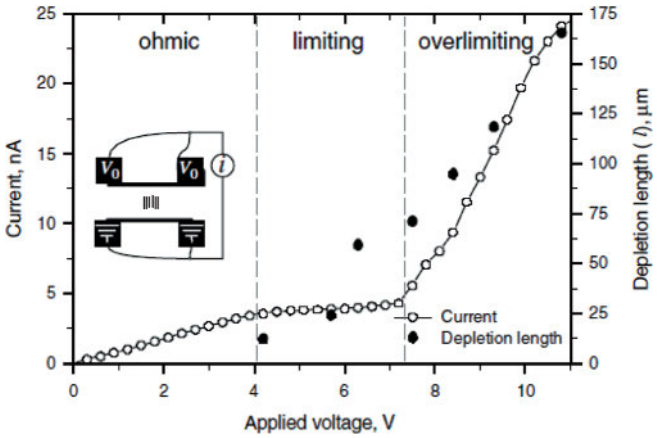

Figure 20. I–V characteristic curve of a cation-exchange nanochannel comprising three distinct regions.[10]

of a cation-exchange nanochannel comprises three distinct regions,[88,89] namely: an initial region, in which the I-V behavior conforms to Ohm′s law; a second region, in which the current saturates with an increasing field strength (i.e., limiting current) due to a reduction toward zero of the ion concentration near the micro/nanochannel interface in the depleted ICP zone;[89] and a third region, in which electroconvection mixing by the vortices reduces the ICP effect and results in an overlimiting current when the applied potential is increased.[90] Recently, we have investigated the effect of the pH value on the ion concentration polarization phenomenon and the nonlinear current-voltage characteristics of a hybrid soda-lime glass micro/nanochannel for a constant KCl salt concentration of about 1 mM. The results show that the ionic conductance of the nanochannel under low concentrations is dominated by the transport of counter-ions. A higher pH

© 2014 Wiley-VCH Verlag GmbH & Co. KGaA, Weinheim

value (i.e., a higher surface charge density) indicates a higher electrical conductance of nanochannel in the Ohmic regime, as shown in Figure 21. The surface charge density of the soda-lime glass, estimated from the modified electrical conductance model of nanochannel, is in agreement with the available data in the literature and the result of the site-dissociation model.[91]

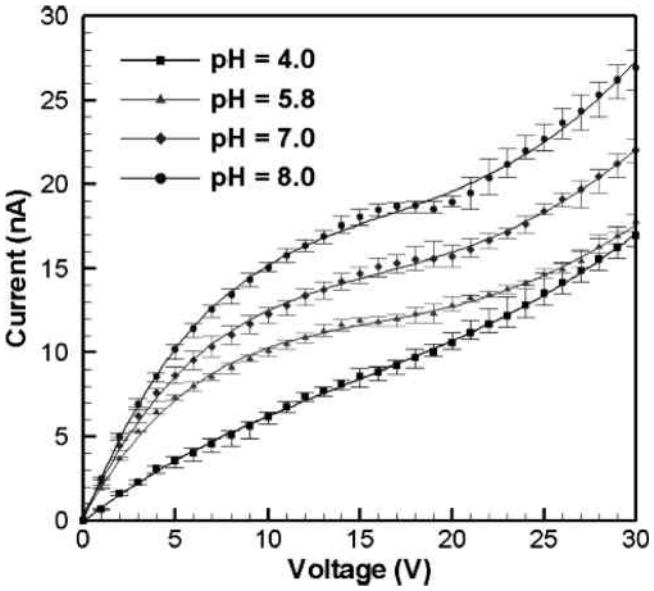

Figure 21. *I–V* characteristic curve of a negatively charged nanochannel, as a function of the pH value, under a constant bulk concentration of about 1 mM.[91]

ICP-related applications include bio-sample preconcentration[85,86] and micro seawater desalination.[20] As shown in Figure 22, ICP prompts the formation of a depletion layer near the interface, which hinders the movement of the charged analytes and therefore creates a sample preconcentration effect on the anodic side. Wang *et al.*[85] presented a microfluidic concentrator, comprising two sample-transportation microchannels connected by a nanochannel to create an ionic depletion/enrichment effect. It was shown that the device was capable of concentrating green fluorescent protein by a factor of 10 million times in 40 minutes. Lee *et al.*[87] proposed a simple method for the fabrication of microfluidic preconcentrators, in which a Nafion ion-selective membrane was patterned on a glass substrate and the substrate was then plasma-bonded to a PDMS microfluidic device. It was shown that a concentration factor as high as 10,000 times could be obtained in around 5 minutes. Kim *et al.*[92] showed that stable electrokinetic trapping can be achieved using heterogeneous ionic hydrogel. Chun *et al.*[93] showed that a negatively-charged hydrogel junction has a high counter-ion selectivity, and can therefore produce a high sample preconcentration intensity. Chen and Yang[94] showed that for a concentrator with a straight microchannel, the time required to achieve a satisfactory preconcentration intensity increases with an increasing channel depth, while for a concentrator with a convergent–divergent microchannel, the preconcentration intensity increases with a reducing convergent channel width. Ko *et al.*[95] developed a preconcentrator comprising a straight microchannel combined with a Nafion membrane (see Figure 23), in which sample concentration was

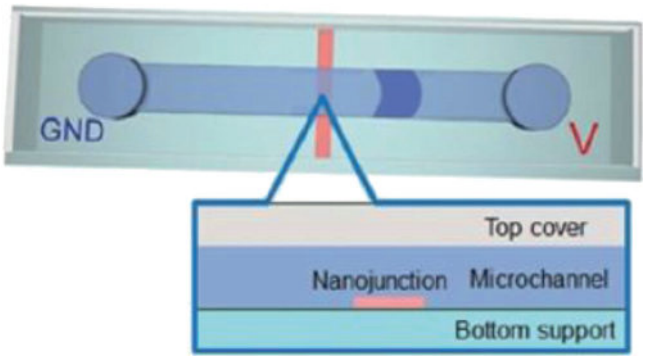

Figure 23. Schematic of preconcentrator comprising straight microchannel and Nafion membrane.[95]

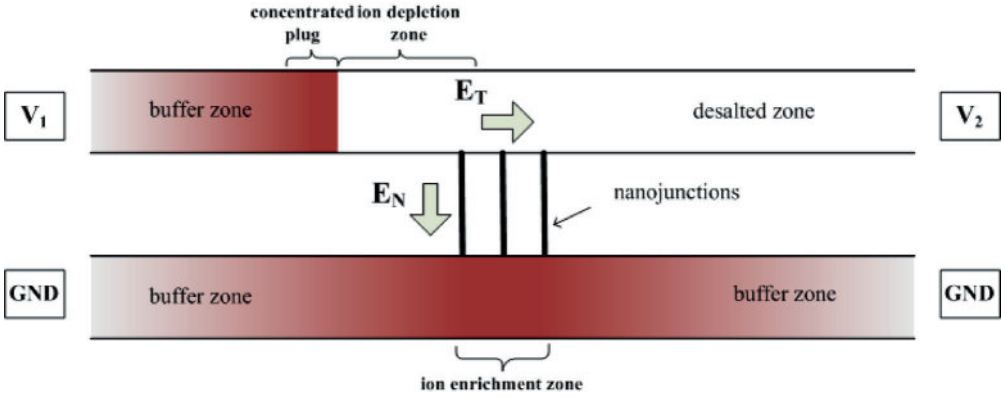

Figure 22. Schematic of preconcentration process in negatively-charged nanochannel.[11]

© 2014 Wiley-VCH Verlag GmbH & Co. KGaA, Weinheim

achieved as a result of the ICP effect induced at the anodic edge of the membrane.

4.4 Water Purification

Water desalination is traditionally performed by means of reverse osmosis (RO). However, such a process is both costly and energy intensive. As a result, electrochemical methods such as electrodialysis (ED),[96] ion concentration polarization,[20,97] and capacitive deionization[98] have attracted increasing interest in recent years.

Electrodialysis is one of the most commonly used membrane-based species-separation processes on account of its scalability, ion controllability and high purification performance.[37] For ED using an ion-selective membrane, an anion exchange membrane (AEM) conducts only anions, while a cation exchange membrane (CEM) conducts only cations. Therefore, the cations and anions in a reservoir can be effectively separated by means of a CEM or AEM and an appropriate electric field. Kwak *et al.*[21] presented a microscale experimental ED platform for visualizing the *in situ* fluid flow and concentration profile for applied voltages in the range of 0–100 V. The results showed that both the fluid flow and the concentration profile showed significant differences between the low current (i.e., Ohmic) regime and the high current (i.e., overlimiting) regime. As shown in Figure 24(a), three distinct current regimes were identified, namely Ohmic (0–2 V), limiting (2–4 V), and overlimiting (4–20 V). In the Ohmic regime, a near-constant resistance occurs, and the resulting linear diffusion induces a linear diffusion boundary layer and stable fluid flow (see Figure 25(a)). In the limiting and overlimiting regimes, an electroconvection effect (i.e., electroosmotic instability) is induced, which results in the formation of both stable and unstable vortices and a depletion zone near the ion exchange membrane (see Figure 25(b)). Figure 24(b) shows the variation in the conductivities of a desalted solution and a concentrated solution, respectively, under the effects of various applied voltages. It can be seen that the conductivity of the desalted solution reduces significantly with increasing voltage. Figure 24(c) shows the fluid flow structures and concentration profile within a channel containing a desalted solution, given the application of different external voltages. The results indicate that the formation of the diffusion boundary layer (DBL) depends strongly on the magnitude of the applied voltage. Given a lower voltage value, the ions are transported mainly by diffusion and drift forces and the DBL is quasi-linearly distributed. However, given a higher applied voltage, the ions are transport-

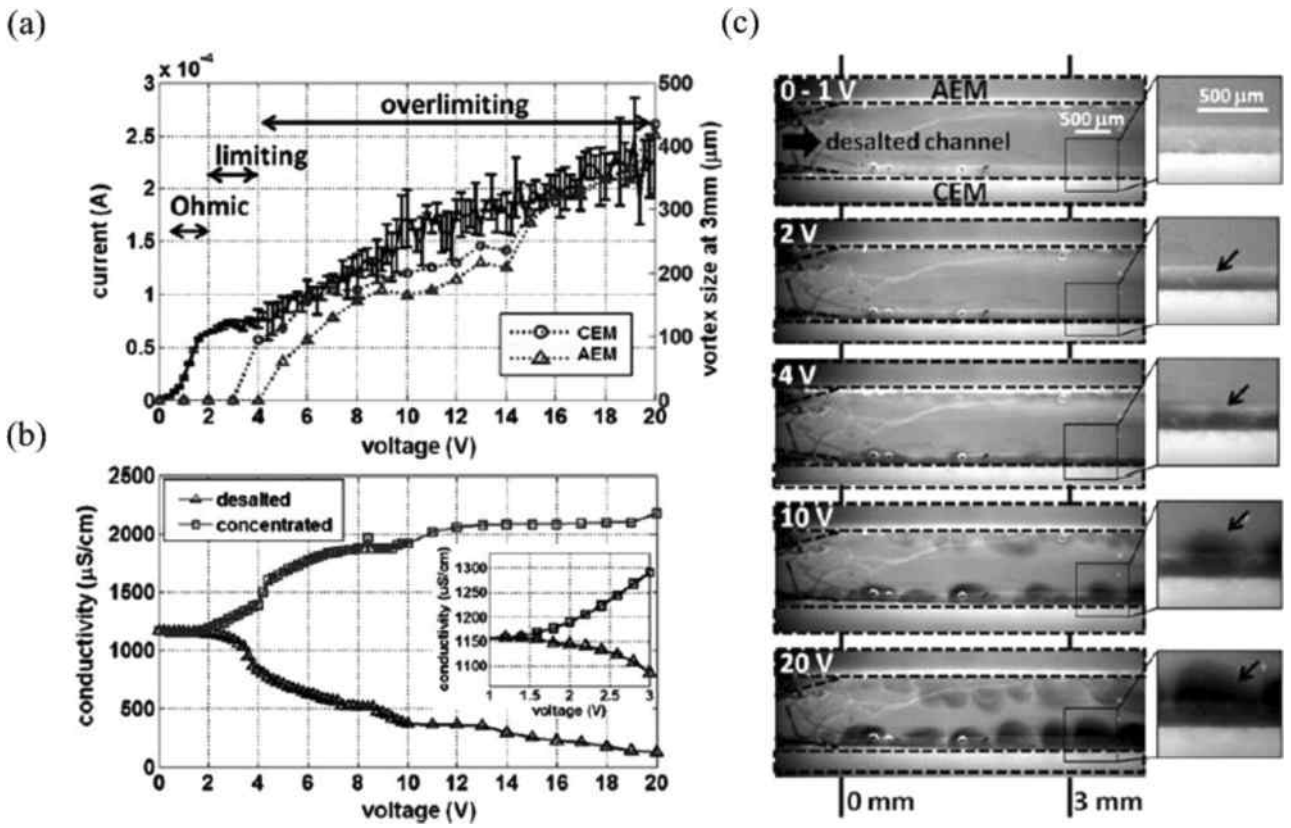

Figure 24. (a) *I–V* curve (solid line with error bars) and vortex size near CEM (dotted line with circles) and AEM (dotted line with triangles). (b) Variation of conductivity of desalted solution and concentrated solution under various applied voltages. (c) Fluid flow visualization results for desalted solution within microchannel given various applied voltages.[21]

© 2014 Wiley-VCH Verlag GmbH & Co. KGaA, Weinheim

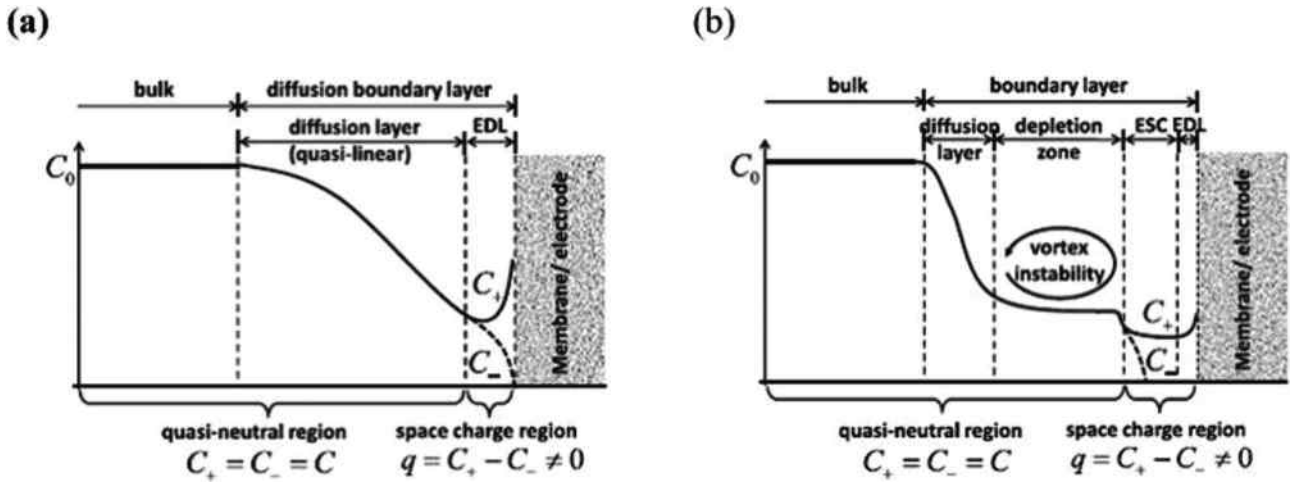

Figure 25. (a) Structure of the diffusion boundary layer and ionic distribution near a micro-/nano-interface, based on the convectional model of the ICP effect under low external applied voltage. (b) Structure of the diffusion boundary layer and ionic distribution, based on the convectional model of the ICP effect under high external applied voltage.[21]

ed by diffusion, drift forces and convection effects, and the DBL is non-linearly distributed. Moreover, vortex generation is observed in the depletion region as a result of the electroconvection effect (see Figure 25(b)). Deng *et al.*[99] performed an experimental investigation into the overlimiting current in porous media. The results showed that the EK phenomena in porous media are essentially nonlinear, and surface conduction and electroosmotic flow both contribute toward the ionic flux due to shock ED under higher voltages. Han *et al.*[20] proposed a device incorporating a Nafion nanojunction for the desalination of water by means of the ICP effect. As shown in Figure 26, in the proposed device, a depletion zone is formed on the high voltage side of the micro-/nano-interface, which repels the salts and any charged species away from the depletion zone and into the inclined channel such that only fresh water is obtained from the horizontal channel. The results showed that the device was capable of removing 99% of the salt content from a saline solution. Compared with the traditional RO process, the proposed device has several important advantages, including lower cost and complexity, and more robust long-term operation without the need to clean or replace the membrane.

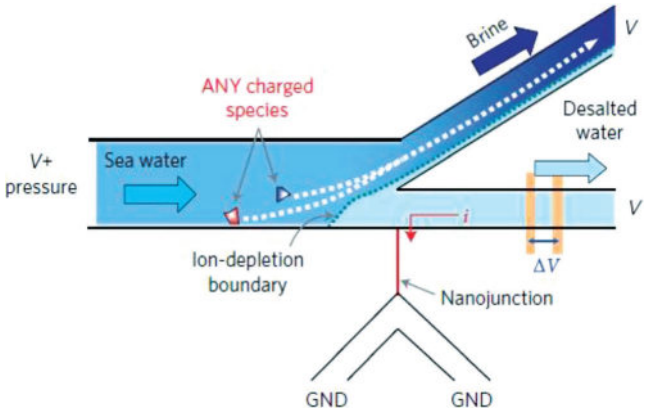

Figure 26. Desalination process using a planar ICP device.[20]

5 Conclusion and Perspectives

This review has described the fundamental phenomena and modeling associated with electrokinetic fluid flow in a nanochannel and at a micro/nanochannel interface. For nanochannels, the surface-to-volume ratio is very high, and therefore various surface-charged-governed transport phenomena occur. When the Debye length is comparable with the nanochannel height, an electrical double layer overlap is formed under low electrolyte concentrations, and the ionic transport is dominated by the surface-charged selectivity, resulting in various phenomena such as the exclusion-enrichment effect and ion concentration polarization. These phenomena provide an effective means of separating and detecting biomolecules for chemical and biomedical engineering purposes. In addition, the ion transport generated in a charged nanochannel provides the means to realize a variety of energy conversion and water desalination devices. As a result, the nanofluidics field has significant potential for the development of life science and engineering applications in the coming years.

Acknowledgement

HC Yeh and RJ Yang gratefully acknowledge the financial support provided to this study by the National Science Council of Taiwan.

© 2014 Wiley-VCH Verlag GmbH & Co. KGaA, Weinheim

References

[1] L. Bocquet, E. Charlaix, *Chem. Soc. Rev.* **2010**, *39*, 1073–1095.
[2] D. Huang, C. Sendner, D. Horinek, R. Netz, L. Bocquet, *Phys. Rev. Lett.* **2008**, *101*, 226101.
[3] R. B. Schoch, J. Han, P. Renaud, *Rev. Mod. Phys.* **2008**, *8*, 840–875.
[4] J. C. T. Eijkel, A. van den Berg, *Chem. Soc. Rev.* **2009**, *39*, 957–973.
[5] J. C. T. Eijkel, A. van den Berg, *Microfluid. Nanofluid.* **2005**, *1*, 249–267.
[6] H. Daiguji, *Chem. Soc. Rev.* **2010**, *39*, 901–911.
[7] J. Israelachvili, *Intermolecular and Surface Force*, 2nd Ed., Academic Press, London, **1992**.
[8] T. A. Zangle, A. Mani, J. G. Santiago, *Chem. Soc. Rev.* **2010**, *39*, 1014–1035.
[9] A. Plecis, R. B. Schoch, P. Renaud, *Nano Lett.* **2005**, *5*, 1147–1155.
[10] S. J. Kim, Y.-C. Wang, J. H. Lee, H. Jang, J. Han, *Phys. Rev. Lett.* **2007**, *99*, 044501.
[11] S. J. Kim, Y.-K. Song, J. Han, *Chem. Soc. Rev.* **2010**, *39*, 912–922.
[12] G. Pardon, W. ven der Wijngaart, *Adv. Colloid Interface Sci.* **2013**, *199–200*, 78–94.
[13] Y. Wang, K. Pant, Z. Chen, G. Wang, W. F. Diffey, P. Ashley, S. Sundaram, *Microfluid. Nanofluid.* **2009**, *7*, 683–696.
[14] Y.-C. Wang, J. Han, *Lab Chip* **2008**, *8*, 392–394.
[15] C. C. Chang, R. J. Yang, *Appl. Phys. Lett.* **2011**, *99*, 083102.
[16] H. Daiguji, Y. Oka, K. Shirono, *Nano Lett.* **2005**, *5*, 2274–2280.
[17] L. J. Chen, L. J. Guo, *Chem. Soc. Rev.* **2010**, *39*, 923–938.
[18] X. Xuan, D. Li, *J. Power Sources* **2006**, *156*, 677–684.
[19] C. C. Chang, R. J. Yang, *Microfluid. Nanofluid.* **2010**, *9*, 225–241.
[20] S. J. Kim, S. H. Ko, K. H. Kang, J. Han, *Nat. Nanotechnol.* **2010**, *5*, 297–301.
[21] R. Kwak, G. Guan, W. K. Peng, J. Han, *Desalination* **2013**, *308*, 138–146.
[22] S. K. Vajandar, D. Xu, J. Sun, D. A. Markov, W. H. Hofmeister, D. Li, *J. Microelectromech. Syst.* **2009**, *18*, 1173–1183.
[23] Z. Xu, J. Miao, N. Wang, W. Wen, P. Sheng, *Phys. Rev. E: Stat. Nonlinear Soft Matter Phys.* **2011**, *83*, 066303.
[24] M. Wang, C. C. Chang, R. J. Yang, *J. Chem. Phys.* **2010**, *132*, 024701.
[25] R. Kwak, V. S. Pham, K. M. Lim, J. Han, *Phys. Rev. Lett.* **2013**, *110*, 114501.
[26] J. P. Rothstein, *Annu. Rev. Fluid Mech.* **2010**, *42*, 89–109.
[27] L. Bocquet, J. L. Barrat, *Soft Matter* **2007**, *3*, 685–693.
[28] L. H. Yeh, S. Xue, S. W. Joo, S. Qian, J. P. Hsu, *J. Phys. Chem. C* **2012**, *116*, 4209–4216.
[29] L. H. Yeh, M. Zhang, S. Qian, *Anal. Chem.* **2013**, *85*, 7527–7534.
[30] C. C. Chang, Y. Kzoe, K. Morikawa, K. Mawatari, R. J. Yang, T. Kitamori, *Anal. Chem.* **2013**, *85*, 4468–4474.
[31] W. Qu, D. Li, *J. Colloid Interface Sci.* **2000**, *224*, 397–407.
[32] T. W. Healy, L. R. White, *Adv. Colloid Interface Sci.* **1978**, *9*, 303–345.
[33] F. Baldessari, J. G. Santiago, *J. Colloid Interface Sci.* **2008**, *325*, 526–538.
[34] D. Stein, M. Kruithof, C. Dekker, *Phys. Rev. Lett.* **2004**, *93*, 035901.
[35] S. Levine, J. R. Marriott, G. Neale, N. Epstein, *J. Colloid Interface Sci.* **1975**, *52*, 136–149.
[36] R. B. Schoch, P. Renaud, *Appl. Phys. Lett.* **2005**, *86*, 253111.
[37] H. Strathmann, *Desalination* **2010**, *264*, 268–288.
[38] R. J. Hunter, *Zeta potential in colloid science principles and applications*, Academic Press, New York, **1981**.
[39] X. Xuan, D. Li, *J. Power Sources* **2006**, *156*, 677–684.
[40] C. C. Chang, R. J. Yang, *J. Colloid Interface Sci.* **2009**, *339*, 517–520.
[41] D. K. Kim, A. Majumdar, S. J. Kim, *Sens. Actuators A* **2007**, *136*, 80–89.
[42] D. K. Kim, D. Kim, S. J. Kim, *J. Micromech. Microeng.* **2008**, *18*, 055006.
[43] B. J. Kirby, E. F. Hasselbrink, Jr., *Electrophoresis* **2004**, *25*, 187–202.
[44] C. L. Rice, R. Whitehead, *J. Phys. Chem.* **1965**, *69*, 4017–4024.
[45] M. R. Davidson, D. J. E. Harvie, *Chem. Eng. Sci.* **2007**, *62*, 4229–4240.
[46] R. P. Bharti, D. J. E. Harvie, M. R. Davidson, *Chem. Eng. Sci.* **2008**, *63*, 3593–3604.
[47] N. A. Mortensen, A. Kristensen, *Appl. Phys. Lett.* **2008**, *92*, 063110.
[48] C. C. Chang, R. J. Yang, M. Wang, J. J. Miau, V. Lebiga, *Phys. Fluids* **2012**, *24*, 072001.
[49] M. Wang, S. Chen, *Commun. Comput. Phys.* **2008**, *3*, 1087–1099.
[50] D. M. Huang, C. Sendner, D. Horinek, R. R. Netz, L. Bocquet, *Phys. Rev. Lett.* **2008**, *101*, 226101.
[51] X. Y. He, S. Y. Chen, G. D. Doolen, *J. Comput. Phys.* **1998**, *42*, 282–300.
[52] M. Wang, N. Pan, J. K. Wang, S. Y. Chen, *Commun. Comput. Phys.* **2007**, *2*, 1055–1070.
[53] Q. S. Zou, X. Y. He, *Phys. Fluids* **1997**, *9*, 1591–1598.
[54] D. Yu, R. Mei, W. Shyy, L. S. Luo, *Phys. Rev. E: Stat. Nonlinear Soft Matter Phys.* **2002**, *65*, 041203.
[55] P. Ewald, *Ann. Phys.* **1921**, *64*, 253–287.
[56] T. Darden, D. York, L. Pedersen, *J. Chem. Phys.* **1993**, *98*, 10089.
[57] J. V. L. Beckers, C. P. Lowe, S. W. de Leeuw, *Mol. Simul.* **1998**, *20*, 369–383.
[58] R. Qiao, N. R. Aluru, *J. Chem. Phys.* **2003**, *118*, 4692–4701.
[59] D. Q. Li, *Electrokinetics in Microfluidics*, Vol. 2, Academic Press, Oxford, **2004**.
[60] M. Wang, J. Liu, S. Y. Chen, *Mol. Simul.* **2007**, *33*, 1273–1277.
[61] J. Liu, M. Wang, S. Chen, M. O. Robbins, *J. Comput. Phys.* **2010**, *229*, 7834–7847.
[62] See Ref. [59].
[63] T. M. Squires, S. R. Quake, *Rev. Mod. Phys.* **2005**, *77*, 977–1026.
[64] F. A. Morrison, J. F. Osterle, *J. Chem. Phys.* **1965**, *43*, 2111–2115.
[65] F. H. J. van der Heyden, D. J. Bonthuis, D. Stein, C. Meyer, C. Dekker, *Nano Lett.* **2006**, *6*, 2232–2237.
[66] J. Eijkel, *Lab Chip* **2007**, *7*, 299–301.
[67] C. Davidson, X. Xuan, *J. Power Sources* **2008**, *179*, 297–300.
[68] Y. Ren, D. Stein, *Nanotechnology* **2008**, *19*, 195707.
[69] R. E. Pattle, *Nature* **1954**, *174*, 660.
[70] F. H. J. van der Heyden, D. Stein, C. Dekker, *Phys. Rev. Lett.* **2005**, *95*, 116104.
[71] D. K. Kim, C. H. Duan, Y. F. Chen, A. Majumdar, *Microfluid. Nanofluid.* **2010**, *9*, 1215–1224.

© 2014 Wiley-VCH Verlag GmbH & Co. KGaA, Weinheim

[72] L. Cao, W. Guo, W. Ma, L. Wang, F. Xia, S. Wang, Y. Wang, L. Jiang, D. Zhu, *Energy Environ. Sci.* **2011**, *4*, 2259–2266.
[73] H. C. Yeh, C. C. Chang, R. J. Yang, *RCS Adv.* **2014**, *4*, 2705–2714.
[74] S. Liu, Q. Pu, L. Gao, C. Korzeniewski, C. Matzke, *Nano Lett.* **2005**, *5*, 1389–1393.
[75] H. Daiguji, P. Yang, A. Szeri, A. Majumdar, *Nano Lett.* **2004**, *4*, 2315–2321.
[76] E. C. Yusko, R. An, M. Mayer, *ACS Nano* **2010**, *4*, 477–487.
[77] K. P. Singh, K. Kumari, M. Kumar, *Appl. Phys. Lett.* **2011**, *99*, 113103.
[78] E. Kalman, I. Vlassiouk, Z. Siwy, *Adv. Mater.* **2008**, *20*, 293–297.
[79] M. Gracheva, D. Melnikov, J. Leburton, *ACS Nano* **2008**, *2*, 2349–2355.
[80] S. Nam, M. Rooks, K.-B. Kim, S. Rossnagel, *Nano Lett.* **2009**, *9*, 2044–2048.
[81] Y. Liu, D. E. Hubber, V. Tabard-Cossa, R. W. Dutton, *Appl. Phys. Lett.* **2010**, *97*, 143109.
[82] B. Jung, R. Bharadwaj, J. G. Santiago, *Electrophoresis* **2003**, *24*, 3476–3483.
[83] B. Jung, R. Bharadwaj, J. G. Santiago, *Anal. Chem.* **2006**, *78*, 2319–2327.
[84] D. Ross, L. E. Locascio, *Anal. Chem.* **2002**, *74*, 2556–2564.
[85] Y. C. Wang, A. L. Stevens, J. Y. Han, *Anal. Chem.* **2005**, *77*, 4293–4299.
[86] K. D. Huang, R. J. Yang, *Electrophoresis* **2008**, *29*, 4862–4870.
[87] J. H. Lee, Y. A. Song, J. Han, *Lab Chip* **2008**, *8*, 596–601.
[88] I. Rubinstein, L. Shtilman, *J. Chem. Soc. Faraday Trans. 2* **1979**, *75*, 231–246.
[89] G. Yossifon, P. Mushenheim, Y.-C. Chang, H.-C. Chang, *Phys. Rev. E: Stat. Nonlinear Soft Matter Phys.* **2009**, 046305.
[90] I. Rubinstein, B. Zaltzman, *Phys. Rev. E: Stat. Phys. Plasmas Fluids Relat. Interdiscip. Top.* **2000**, *62*, 2238–2251.
[91] C. C. Chang, C. P. Yeh, R. J. Yang, *Electrophoresis* **2012**, *33*, 758–764.
[92] P. Kim, S. J. Kim, J. Han, K. Y. Suh, *Nano Lett.* **2010**, *10*, 16–23.
[93] H. G. Chun, T. D. Chung, J. M. Ramsey, *Anal. Chem.* **2010**, *82*, 6287–6292.
[94] C. L. Chen, R. J. Yang, *Electrophoresis* **2012**, *33*, 751–757.
[95] S. H. Ko, Y.-A. Song, S. J. Kim, M. Kim, J. Han, K. H. Kang, *Lab Chip* **2012**, *12*, 4472–4482.
[96] V. Nikonenko, N. Pismenskaya, E. Belova, P. Sistat, P. Huguet, G. Pourcelly, C. Larchet, *Adv. Colloid Interface Sci.* **2010**, *160*, 101–123.
[97] K. D. Huamg, R. J. Yang, *Nanotechnology* **2007**, *18*, 115701.
[98] S. Porada, R. Zhao, A. van der Wal, V. Presser, P. Biesheuvel, *Prog. Mater. Sci.* **2013**, *58*, 1388–1442.
[99] D. Deng, E. V. Dydek, J.-H. Han, S. Schlumpberger, A. Mani, B. Zaltzman, M. Z. Bazant, *Langmuir* **2013**, *29*, 16167–16177.

Received: April 30, 2014
Accepted: July 14, 2014
Published online: September 26, 2014

© 2014 Wiley-VCH Verlag GmbH & Co. KGaA, Weinheim